

# Systematical shell-model calculation in the pairing-plus-multipole Hamiltonian with a monopole interaction for the $pf_{5/2}g_{9/2}$ shell

K. Kaneko\*

*Department of Physics, Kyushu Sangyo University, Fukuoka 813-8503, Japan*

T. Mizusaki

*Institute of Natural Sciences, Senshu University, Tokyo 101-8425, Japan*

Y. Sun<sup>†</sup>

*Department of Physics and Astronomy, Shanghai Jiao Tong University, Shanghai 200240, China  
Collaborative Innovation Center of IFSA (CICIFSA), Shanghai Jiao Tong University, Shanghai 200240, China and  
State Key Laboratory of Theoretical Physics, Institute of Theoretical Physics,  
Chinese Academy of Sciences, Beijing 100190, China*

S. Tazaki

*Department of Applied Physics, Fukuoka University, Fukuoka 814-0180, Japan*

The recently-proposed effective shell-model interaction, the pairing-plus-multipole Hamiltonian with the monopole interaction obtained by empirical fits starting from the monopole-based universal force (PMMU), is systematically applied to nuclei of the  $pf_{5/2}g_{9/2}$  shell region. It is demonstrated that the calculation describes reasonably well a wide range of experimental data, including not only the low-lying and high-excitation spectra,  $E2$  transitions, quadrupole moments, and magnetic moments, but also the binding energies, for Ni, Cu, Zn, Ga, Ge, As, and Se isotopes with  $A = 64 - 80$ . In particular, a structure of the neutron-rich Ge and Se isotopes is discussed in detail.

PACS numbers: 21.10.Dr, 21.60.Cs, 21.60.Jz, 21.10.Re

## I. INTRODUCTION

Nuclei in the  $pf_{5/2}g_{9/2}$  shell, i.e. those with nucleon numbers between the magic numbers 28 and 50, show at least two attractive properties. The first one is a structure variation around the semi-magic shell-closure at  $N = 40$ . It has been known that the  $Z = 28$  isotone  $^{68}\text{Ni}$  has one of the main characters of a double closed-shell nucleus [1, 2], and isomers have been found in the neighborhood of this nucleus. The lowered first excited  $0_2^+$  state in  $^{68}\text{Ni}$  is interpreted so as to support the magicity. However,  $^{68}\text{Ni}$  does not exhibit an irregularity in two-neutron separation energy as expected for magic nuclei [3]. It has been shown that this contradiction can be understood by the parity change across the  $N = 40$  shell gap [3–6]. Moving to heavier isotones of  $N = 40$  with increasing proton number, there have been many experimental evidences suggesting an increasing collectivity, for example those in the Ge [7, 8] and Se isotopes [9–12]. With  $Z$  approaching 40, the  $N = Z$  isotone  $^{80}\text{Zr}$  is known to be strongly deformed [13], and signs of a shell closure disappear completely and the nucleus can be regarded as a good rotor.

Another interesting property to be mentioned for the  $pf_{5/2}g_{9/2}$  shell is the shape evolution in the mass-70 region [10–12, 14–16]. In particular, the nuclei around the  $N = Z$  line exhibit a variety of nuclear shapes [17, 18]. Shape changes are sensitive probes of the structure, and the corresponding nuclei

can serve as good testing grounds for shell-model interactions. For example,  $^{64,66,68}\text{Ge}$  were studied using large-scale shell model calculations [19–21]. For  $^{70,72,74,76}\text{Ge}$ , shape changes were discussed with the observed spectroscopic quadrupole moment [22], which were attributed to the large shell gaps at the prolate and oblate deformation for proton and neutron numbers 34 and 36 as seen in the Nilsson diagram. For  $^{68}\text{Se}$ , it was found that the oblate ground-state band coexists with a prolate excited band, forming a shape coexistence phenomenon [16, 18]. Shape coexistence was also investigated for  $^{70,72,74}\text{Se}$  [10–12]. It was reported that in  $^{70}\text{Se}$ , the oblate shape near the ground state evolves quickly to a prolate shape at higher spins [10]. Further experiments suggested that in  $^{72}\text{Se}$ , there is no well-defined shape for the lowest levels due to shape mixings [11], and the low-lying states in  $^{74}\text{Se}$  show coexistence of spherical and prolate shapes [12].

Various theoretical approaches based on deformed mean-fields have been applied to this mass region [23–27]. On the other hand, shell-model calculations using different effective interactions, such as JUN45 [21] and JJ4B [28–30] for the  $pf_{5/2}g_{9/2}$  model space, have also been reported. In principle, interactions for nuclear shell-model calculations should be derived microscopically from the free nucleon-nucleon forces [31, 32] and also the three-body nucleon forces [33]. However, it has been shown that such effective interactions fail to describe nuclear properties such as binding energies, excitation spectra, and  $E2$  transitions once the number of valence nucleons becomes large. Therefore, considerable effort has been put forward to construct effective interactions for different shell-model spaces [5, 28–30, 34–38]. For the JUN45 and JJ4B effective interactions, the starting point for the fit-

\*Electronic address: kaneko@ip.kyusan-u.ac.jp

<sup>†</sup>Electronic address: sunyang@sjtu.edu.cn

ting procedure is a realistic G-matrix interaction based on the Bonn-C  $NN$  potential and core-polarization corrections with a  $^{56}\text{Ni}$  core. With the inclusion of the proton  $f_{7/2}$  and neutron  $d_{5/2}$  orbitals, in addition, the LNPS [5, 38] interaction based on the Kuo-Brown interaction including the Kahana-Lee-Scott potential [39] has also been proposed.

Among the effective interactions, the pairing plus quadrupole-quadrupole ( $P+QQ$ ) interaction [40, 41] has been widely applied to describe various nuclear properties, such as excitation energies, moments, transitions, and reaction rates, for a wide range of nuclei in the medium to heavy mass regions. This interaction is represented by two basic components, the pairing and quadrupole forces as the short and long range parts of the interaction, respectively. Dufour and Zuker have shown that any realistic effective interaction is dominated by the  $P+QQ$  interaction with the monopole terms [42]. It has been understood that, while the pairing and quadrupole terms take care of the main and smooth part of the structure properties, the monopole terms play important roles for the shell evolution and are often responsible for explaining anomalous behaviors in spectra and transitions. It has been shown that the extended  $P+QQ$  model with the monopole interaction ( $EPQQM$ ) works surprisingly well for the  $N \approx Z$  nuclei [19, 43], where the monopole terms are treated as corrections. The strength parameters in  $EPQQM$  have been chosen so as to fit the known data. In a series of publications, we have found that the monopole terms are important to account for the unusual shell evolution in the neutron-rich region. The model has also demonstrated its capability of describing the microscopic structure in different  $N \approx Z$  nuclei, as for instance, in the  $pf$ -shell [43] and the  $pf_{5/2g_{9/2}}$ -shell regions [19]. It has been shown that this model is also applicable for the neutron-rich nuclei in the  $fpg$ -shell region [44] and the  $sd$ - $pf$  shell region [45]. Quite recently, the  $EPQQM$  model has also been successfully applied to the neutron-rich nuclei around  $^{132}\text{Sn}$  [46–49].

One of the important issues in nuclear structure is persistence or disappearance of the traditional magic numbers when moving away from the  $\beta$ -stability line. It has been known that the conventional magic numbers disappear in some cases of the neutron-rich region, but new magic numbers may emerge. For example, the neutron-rich nuclei  $^{12}\text{Be}$ ,  $^{32}\text{Mg}$ , and  $^{42}\text{Si}$  were found to exhibit large collectivity in spite of the corresponding neutron magic numbers  $N = 8, 20, \text{ and } 28$ . The monopole interaction is the key ingredient for explaining the binding energies, the emergent magic numbers, and the shell evolution in the neutron-rich region. The connection between the monopole interaction and the tensor force [50] was confirmed within the self-consistent mean-field model using the Gogny force [51]. Thus one of the physical origins of the monopole interaction was attributed to the tensor force [50] which explains the shell evolution. This explanation is an important development in understanding the structure of unknown mass regions. Recently, general properties of the monopole components of the effective interactions have been presented through introducing the monopole-based universal interaction [52], which consists of simple central and tensor forces and can produce a variety of shell evolution across dif-

ferent mass regions. It has been shown that the monopole matrix elements obtained from this interaction are in good agreement with those of the SDFP-M in the  $sd$  shell and of the GXPF1A in the  $pf$  shell [34]. The monopole-based universal interaction seems to be really a universal one, applicable for different nuclear shell regions. Thus it is of a great interest to perform shell-model calculations with the pairing and multipole interactions, starting from the monopole part constructed from the monopole-based universal interaction.

The present authors have recently proposed a unified realistic shell-model Hamiltonian called PMMU [53], employing the  $P+QQ$  Hamiltonian with the monopole interaction  $V_m^{MU}$  constructed from the monopole-based universal force. It was demonstrated [53] that PMMU describes well nuclear properties of the  $pf$  and  $pf_{5/2g_{9/2}}$  shell nuclei, such as systematics of the first excited  $2^+$  states and  $B(E2)$  values, and detailed energy spectrum for  $^{56}\text{Ni}$ ,  $^{72}\text{Ge}$ ,  $^{55}\text{Co}$ , and  $^{69}\text{Ge}$ . It is now important to investigate general nuclear properties for a considerable amount of nuclei including binding energies, detailed energy levels, and  $E2$  transitions, to confirm further the reliability of the PMMU model. The present article is a comprehensive work following Ref. [53], and we perform large-scale shell-model calculations systematically for nuclei in the  $pf_{5/2g_{9/2}}$  model space. We shall show that starting from the monopole interaction  $V_m^{MU}$ , a set of 28 parameters including four  $P+QQ$  force strengths, 14 monopole matrix elements, and four single-particle energies are determined by refitting to the experimental binding energies of 91 nuclei with the mass  $A = 64 - 80$ . Data for excited states are also used to fit these parameters. We will discuss the shell evolution, binding energies, excited energy spectrum and  $E2$  transitions. Thus, the main purpose of the present work is to test the PMMU model for a wide range of nuclei in the  $pf_{5/2g_{9/2}}$  shell region, with a particular attention paid to the structure of Ge and Se isotopes.

The paper is arranged as follows. In Sec. II, we outline our model. In Section III, we present the model parameters with the detailed fitting procedure and description of binding energies. The rest sections are devoted to discussion of the results: the structure of low-lying states are discussed in Section IV and structure of highly excited states in Ge and Se isotopes are presented in Section V. Finally, summary and conclusions are given in Section VI.

## II. THE PMMU MODEL

The Hamiltonian of the PMMU model, proposed by the present authors in Ref. [53], takes the following form

$$\begin{aligned}
 H &= H_0 + H_{PM} + H_m, \quad (1) \\
 H_0 &= \sum_{\alpha} \epsilon_{\alpha} c_{\alpha}^{\dagger} c_{\alpha}, \\
 H_{PM} &= - \sum_{J=0,2} \frac{1}{2} g_J \sum_{M\kappa} P_{JM1\kappa}^{\dagger} P_{JM1\kappa} \\
 &\quad - \frac{1}{2} \chi_2 \sum_M : Q_{2M}^{\dagger} Q_{2M} : - \frac{1}{2} \chi_3 \sum_M : O_{3M}^{\dagger} O_{3M} : \\
 H_m &= \sum_{a \leq b, T} V_m(ab, T) \sum_{JMK} A_{JMTK}^{\dagger}(ab) A_{JMTK}(ab),
 \end{aligned}$$

where  $H_0$  is the single-particle Hamiltonian,  $H_{PM}$  the pairing plus multipole term, and  $H_m$  the monopole term. For  $H_{PM}$ , we take the  $J = 0$  and  $J = 2$  forces in the pairing channel, and the quadrupole-quadrupole ( $QQ$ ) and octupole-octupole ( $OO$ ) forces in the particle-hole channel [19, 43]. Higher order pairing and multipole terms can be added if necessary. The monopole matrix elements  $V_m(ab, T)$  in  $H_m$  are defined as [54]

$$V_m(ab, T) = \frac{\sum_J (2J+1) V_{ab,ab}^{JT}}{\sum_J (2J+1)}, \quad (2)$$

where  $V_{ab,ab}^{JT}$  are the diagonal matrix elements between the two-nucleon states coupled to angular momentum  $J$  and isospin  $T$ . The monopole interaction has connections with the tensor force, which generally explains the shell evolution [51]. It was pointed out that the three-nucleon forces in the monopole interaction are also important for neutron-rich nuclei [52, 55, 56]. Recently, Otsuka *et al.* have discussed universal properties of the monopole interaction in the effective interaction [57] and suggested the so-called monopole-based universal force [52] as an  $NN$  potential,  $V_{MU}$ , which consists of the Gaussian central force and the tensor force. The  $V_{MU}$  force has been successfully applied to light nuclei [58, 59] and somewhat heavier ones [60].

In a recent publication [53], we have proposed a unified realistic shell-model Hamiltonian employing the pairing plus multipole Hamiltonian with the monopole interaction constructed from  $V_{MU}$ , subject to modifications through fitting the known experimental data. The monopole-based universal force consists of two terms, the Gaussian central force and the tensor force

$$V_{MU} = V_{\text{central}} + V_{\text{tensor}}, \quad (3)$$

with

$$\begin{aligned}
 V_{\text{central}} &= \sum_{S,T} f_{S,T} P_{S,T} \exp(-(r/\mu)^2), \\
 V_{\text{tensor}} &= (\vec{\tau}_1 \cdot \vec{\tau}_2) ([\vec{s}_1 \vec{s}_2]^{(2)} \cdot Y^{(2)}) g(r),
 \end{aligned}$$

where  $S(T)$  means spin (isospin),  $P$  denotes the projection operator onto the channels  $(S, T)$  with strength  $f$ , and  $r$  and  $\mu$

are the internucleon distance and Gaussian parameter, respectively. Here  $\vec{\tau}_{1,2}$  ( $\vec{s}_{1,2}$ ) denotes the isospin (spin) of nucleons. In the central force, the Gaussian parameter is fixed to be  $\mu = 1.0$  fm, and the strength parameters are  $f_{0,0} = f_{1,0} = -166$ ,  $f_{0,1} = -99.6$ , and  $f_{1,1} = 132.8$  (all in MeV). The  $\pi + \rho$  meson exchange force is used for the strength  $g(r)$  [51]. Figure 1 illustrates the triplet-even potential due to the Gaussian central force  $V_{\text{central}}$  and the tensor force  $V_{\text{tensor}}$  with the above parameters. The monopole Hamiltonian  $H_m$  in Eq. (1) can then be rewritten in the known form [54, 61]

$$H_m = \sum_{a \leq b} \left[ r_{ab} \hat{n}_a (\hat{n}_b - \delta_{ab}) + s_{ab} (\hat{T}_a \cdot \hat{T}_b - \frac{3}{4} \hat{n}_a \delta_{ab}) \right], \quad (4)$$

with

$$\begin{aligned}
 r_{ab} &= \frac{3V_m(ab, T=1) + V_m(ab, T=0)}{4(1 + \delta_{ab})}, \\
 s_{ab} &= \frac{V_m(ab, T=1) - V_m(ab, T=0)}{1 + \delta_{ab}}.
 \end{aligned}$$

## III. THE PMMU INTERACTION AND THE GROUND STATE DESCRIPTION

In this section and the two subsequent sections, we present the results obtained from systematical shell-model calculations with the PMMU model, and compare the results with available experimental data. The present section discusses how the PMMU interaction parameters are determined. The two subsequent sections are devoted to discussions of systematical calculations for low-lying states and for states of high excitations, respectively. Most of the shell-model calculations shown in the present paper are carried out by using the shell-model code MSHELL64 [62], which enables calculations with a M-scheme dimension up to  $\sim 3 \times 10^9$ .

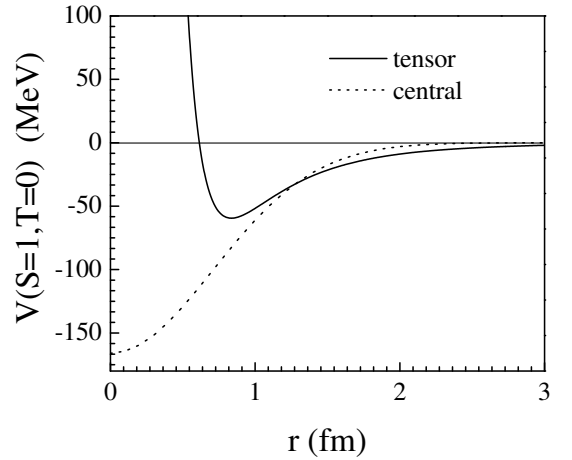


FIG. 1: Triplet-even potential due to the central force and the tensor force.

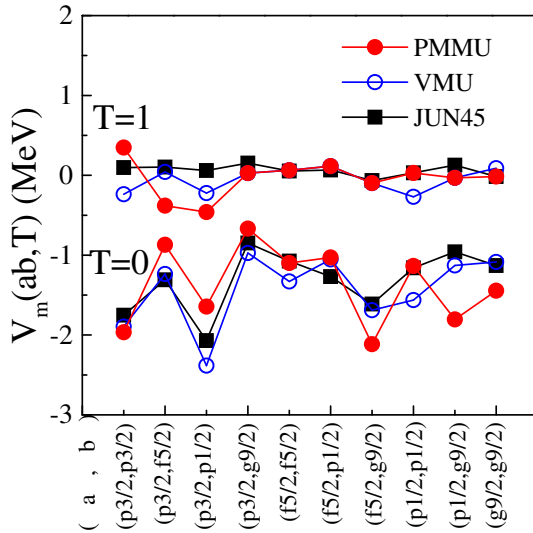


FIG. 2: (Color online) Comparison of the monopole matrix elements  $V_m(ab, T)$  among the effective interactions JUN45, VMU, and PMMU.

### A. Determination of the PMMU interaction

In Ref. [53], we have shown that the PMMU model is successful in describing energy levels and  $E2$  transitions for a large number of nuclei in the  $pf$ - and  $pf_{5/2}g_{9/2}$ -shell regions. In this paper, we consider  $pf_{5/2}g_{9/2}$  as the model space. Starting from the monopole interaction  $V_m^{MU}$ , a set of 28 parameters, which include the four strengths for the pairing-plus-multipole forces, twenty for the monopole matrix elements, and four single-particle energies, are determined by fitting to the known experimental data of 91 nuclei. These nuclei are taken from the mass region with  $A = 64 - 80$ , including  $^{64-76}\text{Ni}$ ,  $^{64-78}\text{Cu}$ ,  $^{65-80}\text{Zn}$ ,  $^{66-80}\text{Ga}$ ,  $^{69-80}\text{Ge}$ ,  $^{67-78}\text{As}$ , and  $^{73-80}\text{Se}$ . For the Ni, Cu, Zn, Ga, and Ge isotopes, calculations are performed without any truncation, while for As and Se isotopes, some truncations have to be introduced.

The detailed fitting procedure carried out in Ref. [53] is as follows. We take the pairing plus multipole Hamiltonian, and for the monopole part, we start from  $V_m^{MU}(ab, T)$  constructed by the monopole-based universal force of Otsuka *et al.* [52] and modify the monopole matrix elements so as to fit the experimental data. The experimental yrast states of the even-even Zn, Ge and Se isotopes and the low-lying  $1/2^-$ ,  $3/2^-$ ,  $5/2^-$ , and  $9/2^+$  states of the odd-mass Ni, Zn, Ge, Se are considered for the fitting. In total, 91 binding energy data and 186 experimental energies of excited states from these 91 nuclei are taken in the fitting procedure. For example, the four pairing-plus-multipole force strengths, the four single-particle energies, and the  $T = 1$  matrix elements  $V_m^{MU}(p_{3/2}, f_{5/2}, T = 1)$ ,  $V_m^{MU}(p_{3/2}, p_{3/2}, T = 1)$ , and  $V_m^{MU}(p_{3/2}, p_{1/2}, T = 1)$  are modified to fit mainly the yrast energy levels for  $^{60-64}\text{Zn}$  and  $^{64-68}\text{Ge}$ . The  $T = 0$  matrix elements are adjusted to fit the binding energies of the nuclei with  $28 \leq Z \leq 34$  and  $30 \leq N \leq 50$ . As a result, the rms de-

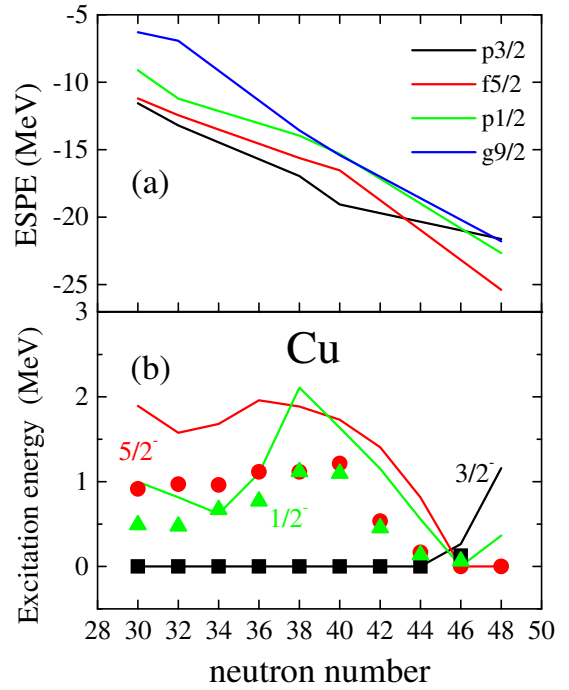


FIG. 3: (Color online) (a) Effective single-particle energies of proton orbits for Cu isotopes. (b) Comparison of the energy levels of the lowest  $3/2^-$ ,  $5/2^-$ , and  $1/2^-$  states for odd-mass Cu isotopes. The filled symbols and the lines are the experimental data and the shell-model results, respectively. Experimental data are taken from Ref. [63].

viations for binding and excitation energies (see discussions below) are 691 keV and 256 keV, respectively.

All together, a total of 14 monopole terms are modified from the original  $V_m^{MU}$ , and all the monopole matrix elements are scaled by a factor  $(58/A)^{0.3}$  for the calculation with the present model space. The modified monopole matrix elements, denoted as  $V_m^{\text{PMMU}}$ , are shown in Fig. 2. The original monopole matrix elements,  $V_m^{MU}$ , are also displayed in the same figure, which are found for most cases to be closer to those of the JUN45 effective force [21]. Thus from Fig. 2, it can be seen that our fitted  $V_m^{\text{PMMU}}$  is clearly different from the original one in the following matrix elements:  $V_m^{MU}(p_{3/2}, p_{1/2}, T = 0)$ ,  $V_m^{MU}(f_{5/2}, g_{9/2}, T = 0)$ ,  $V_m^{MU}(p_{3/2}, f_{5/2}, T = 0)$ ,  $V_m^{MU}(g_{9/2}, g_{9/2}, T = 0)$ ,  $V_m^{MU}(p_{1/2}, p_{1/2}, T = 0)$  and  $V_m^{MU}(p_{1/2}, g_{9/2}, T = 0)$  for  $T = 0$ , and  $V_m^{MU}(p_{3/2}, f_{5/2}, T = 1)$ ,  $V_m^{MU}(p_{3/2}, p_{3/2}, T = 1)$  and  $V_m^{MU}(p_{3/2}, p_{1/2}, T = 1)$  for  $T = 1$ .

The modifications of the  $T = 0$  monopole matrix elements between the  $fp$  shell and the  $g_{9/2}$  orbit are particularly important for the shell evolutions seen in the shell-structure changes due to the filling of specific single-particle orbits. The single-particle energies and interaction strengths in Eq. (1) are taken

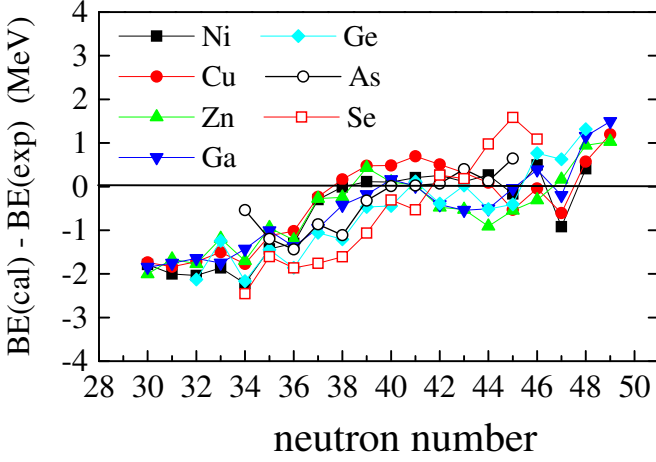


FIG. 4: (Color online) Deviations of the calculated binding energies from the experimental data for  $Z = 28 - 34$  as functions of neutron number. Data are taken from Ref. [64].

from Ref. [53] as follows (all in MeV)

$$\begin{aligned} \varepsilon_{p_{3/2}} &= -9.40, \varepsilon_{f_{5/2}} = -8.29, \varepsilon_{p_{1/2}} = -7.49, \\ \varepsilon_{g_{9/2}} &= -5.70, \\ g_0 &= 18.0/A, \quad g_2 = 0.0, \\ \chi_2 &= 334.0/A^{5/3}, \quad \chi_3 = 259.2/A^2. \end{aligned} \quad (5)$$

The modifications for the  $T = 0$  monopole matrix elements  $V_m^{\text{PMMU}}(f_{5/2}, g_{9/2}, T = 0)$  and  $V_m^{\text{PMMU}}(p_{1/2}, g_{9/2}, T = 0)$  cause significant shell-variations with increasing neutron number. The proton effective single-particle energies (ESPE) as a function of neutron number are shown in Fig. 3 (a). Due to the large difference between the  $T = 0$  matrix elements  $V_m^{\text{PMMU}}(p_{3/2}, g_{9/2}, T = 0)$  and  $V_m^{\text{PMMU}}(f_{5/2}, g_{9/2}, T = 0)$ , the ESPE of the proton  $f_{5/2}$  orbit is pushed down drastically relative to the  $p_{3/2}$  orbit as the neutron  $g_{9/2}$  orbit is occupied for  $N > 40$ , and becomes lower than the other orbits for  $N > 46$ . This shell variation reflects the behavior of the low-lying  $5/2^-$  energy level of Cu isotopes as shown in Fig. 3 (b), where the calculation reproduces the experimental data reasonably. As another example, the experimentally observed feature of the near-degeneracy of the  $5/2^-$  and  $1/2^-$  states for  $N > 40$  is reproduced very well. This is due to the large  $T = 0$  matrix element  $V_m^{\text{PMMU}}(p_{1/2}, g_{9/2}, T = 0)$ , which is adjusted to have a similar magnitude to the one of  $V_m^{\text{PMMU}}(f_{5/2}, g_{9/2}, T = 0)$ .

### B. Description of binding energies

The total binding energies are expressed as

$$B(Z, N) = E_{SM}(Z, N) + E_C(Z, N) + BE(^{56}\text{Ni}), \quad (6)$$

where  $E_{SM}(Z, N)$  is the shell-model ground-state energy calculated by the present PMMU model,  $E_C(Z, N)$  the Coulomb

energy, and  $BE(^{56}\text{Ni})$  the binding energy of the  $^{56}\text{Ni}$  core [64]. The Coulomb energy is evaluated by using the empirical formula

$$E_C(\pi, \nu) = \varepsilon_C \pi + \frac{\pi(\pi-1)}{2} V_C + \left(\frac{1}{2}\pi\right) b_C + \Delta_{np} \pi \nu, \quad (7)$$

where  $\pi$  and  $\nu$  denote the numbers of valence protons and neutrons, respectively. We use the parameter set 2 in Table I of Ref. [65], where the values of  $\varepsilon_C$ ,  $V_C$ ,  $b_C$ , and  $\Delta_{np}$  in Eq. (7) are determined so as to fit the observed Coulomb displacement energies for the mass region of  $20 < Z < 42$  and  $32 < N < 50$ .

In Fig. 4, deviations of the calculated binding energies from the experimental values are shown for various isotopic chains as functions of neutron number  $N$ . All the results are obtained by the shell-model calculations without any truncation for Ni, Cu, Zn, Ga, Ge, As, and Se isotopes. The binding energies of As and Se isotopes are calculated for  $N = 33, 34, 48, 49$  and  $N = 34, 35, 48, 49$ , respectively. The overall agreement with data is quite good for the entire mass range included in the fitting ( $A = 58 - 83$ ), except that one finds relatively large deviations for nuclei below  $N = 36$  where the calculations give an overbinding. One can expect that the calculation may also be applicable to other nuclei that have not been included in the fitting procedure.

## IV. STRUCTURES OF LOW-LYING STATES

To test the validity of a new effective shell-model interaction, it is important to examine it through systematical calculations for the low-lying states of many nuclei. In this section, the first excited  $0_2^+$ ,  $2_1^+$ ,  $4_1^+$  states, and other low-lying states are discussed.

### A. Systematics of excited $2_1^+$ , $4_1^+$ , and $0_2^+$ states

The systematics of the  $2_1^+$ ,  $4_1^+$  and  $0_2^+$  states are studied for a wide range of even-even nuclei in this mass region. Figure 5 shows the excitation energies of these states for Ni, Zn, Ge, and Se isotopes. The lightest isotope in each isotopic chain is taken to be the one with  $N = Z$ . Overall, the calculations reproduce the experimental data fairly well. The common discrepancy of the calculation is that beyond  $N = 40$  in each isotopic chain, the theoretical  $2_1^+$  energies are higher than the experimental ones. This would suggest that the present model space is insufficient to describe the systematic behavior beyond  $N = 40$ , possibly due to the missing  $d_{5/2}$  orbit. Other discrepancies are seen in the description of the  $2_1^+$  states of the Ni isotopes and the  $4_1^+$  states of the Zn isotopes. As for the Ni isotopes, the observed excitation energy  $E_x(2_1^+)$  takes the largest value at  $N = 40$  while the calculation shows a peak at  $N = 38$ . These could be attributed to the missing  $f_{7/2}$  orbit in the present model space. If the  $f_{7/2}$  orbit had been included, the attractive  $T = 0$  monopole force between the proton  $f_{7/2}$  and neutron  $p_{1/2}$  orbits would push down the neutron  $p_{1/2}$  orbit, causing an increase of the shell gap between the neutron

$g_{9/2}$  and  $p_{1/2}$  orbits, which could result in a large excitation energy  $E_x(2_1^+)$  at  $N = 40$  as seen in the experiment.

We now focus the discussion on the interesting behavior of the first excited  $0_2^+$  state. As can be seen in Fig. 5, the common feature is that the excitation energy of the  $0_2^+$  states changes drastically along each isotopic chain and reaches the minimum at  $N = 40$ . In particular for  $^{72}\text{Ge}$ , the  $0_2^+$  state lies below the  $2_1^+$  state. Thus this is a mysterious  $0_2^+$  state for the Ge isotopes. There have been many theoretical attempts to explain this behavior. However, most shell model approaches did not succeed to answer this question. The shell-model calculation using the JUN45 effective interaction successfully reproduced the irregular behavior of the  $0_2^+$  state [21]. Comparing the theoretical results and the experimental data shown in Fig. 5, one can see that the present calculation describes correctly the trend of systematics of the  $0_2^+$  states for all the Ni, Zn, Ge, and Se isotopes.

We can explain how this systematical trend is obtained in our calculation. Figure 6 shows the occupation numbers,  $n(vg_{9/2})$ , of the neutron  $g_{9/2}$  orbit in the yrast  $0_1^+$ ,  $2_1^+$ , and  $4_1^+$  states, and in the excited  $0_2^+$  state. As one can see from Fig. 6 (a),  $n(vg_{9/2})$  in all the three yrast states increase monotonously with the neutron number. On the other hand,  $n(vg_{9/2})$  of the  $0_2^+$  state shows a different behavior: the in-

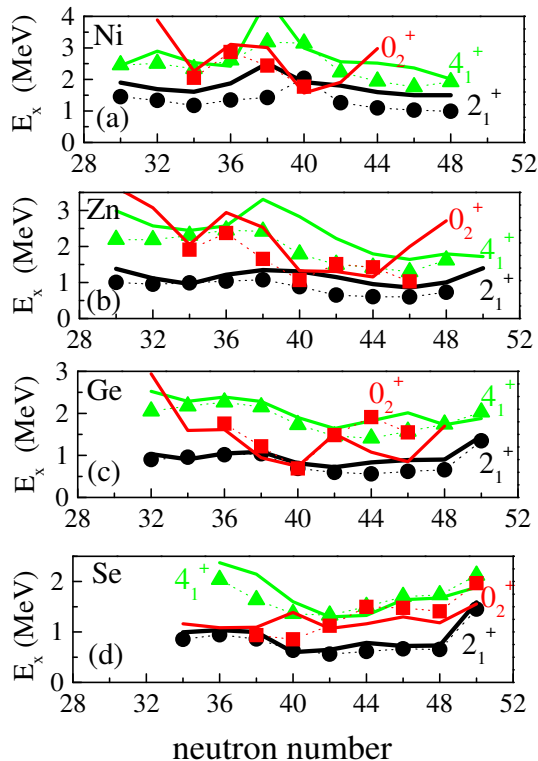


FIG. 5: (Color online) Systematics in the excitation energies of the first excited  $0^+$ ,  $2^+$ , and  $4^+$  states for Ni, Zn, Ge, and Se isotopes. The  $0^+$ ,  $2^+$ , and  $4^+$  states are indicated by the squares, circles, and triangles, respectively. The calculated results are shown by the solid lines with the same colors, and compared with the experimental data taken from Ref. [63].

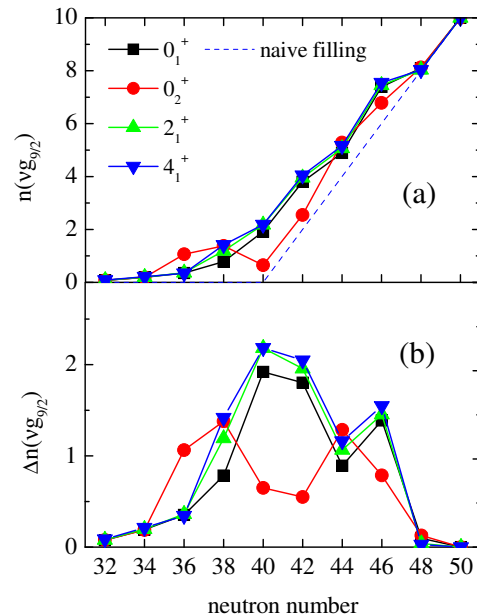


FIG. 6: (Color online) Neutron  $g_{9/2}$  occupancies for the low-lying states in the Ge isotopes. (a) The occupation numbers  $n(vg_{9/2})$  of the low-lying states in the Ge isotopes. The broken line indicates the naive filling configuration. (b) The differences between the neutron occupation numbers and the naive filling configurations.

creasing trend turns back at  $N = 40$  where the minimum is seen. Moreover, the  $n(vg_{9/2})$  curve of the  $0_2^+$  state deviates clearly from the yrast ones at  $N = 40$  and  $42$ , but behaves as the broken line in Fig. 6 (a) that represents the naive filling configuration. The additional occupancy of the  $g_{9/2}$  orbit to the naive filling occupancy  $n(vg_{9/2})_0$ , shown by the broken line in Fig. 6 (a), is considered as a measure of excitation from the  $pf_{5/2}$  shell to the  $g_{9/2}$  orbit. The magnitude of the additional occupancy  $\Delta n(vg_{9/2}) = |n(vg_{9/2}) - n(vg_{9/2})_0|$  can be seen more clearly in Fig. 6 (b). The enhanced excitations of the yrast states increase the collectivity in the isotopes of  $N = 40$  and  $42$ . In contrast, such excitations are largely suppressed for the  $0_2^+$  state in these two isotopes. Thus the magicity of the  $N = 40$  leads to a lowering of the  $0_2^+$  state toward  $N = 40$ . Similar conclusions were given by Ref. [21].

On the other hand, the proton occupation numbers  $n(\pi p_{3/2})$  in the  $p_{3/2}$  orbit are shown in Fig. 7 (a). One sees again the distinct behavior of the  $0_2^+$  state from the  $0_1^+$ ,  $2_1^+$ ,  $4_1^+$  yrast states. For the yrast states,  $n(\pi p_{3/2})$  are around two for the isotopes below  $N = 40$ , but start to decrease with increasing neutron number after  $N = 40$ . As the occupation number for the naive filling configuration is four, two protons are excited from the  $p_{3/2}$  orbit to the upper orbits below  $N = 40$ , and the proton excitation is gradually enhanced starting from  $N = 42$ . For the heavier isotopes, additional protons are excited to the  $f_{5/2}$  orbit, generally because of the deformation and the pair-

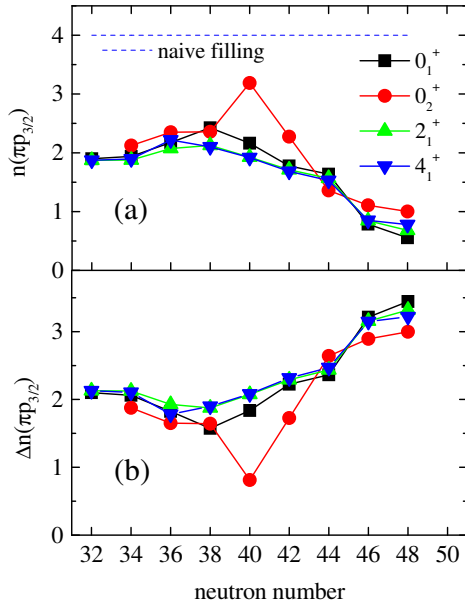


FIG. 7: (Color online) Proton  $p_{3/2}$  occupancies for the low-lying states in the Ge isotopes. (a) The occupation numbers  $n(vp_{3/2})$  of the low-lying states in the Ge isotopes. The broken line indicates the naive filling configuration. (b) The differences between the neutron occupation numbers and the naive filling configurations.

ing effect. For the excited  $0_2^+$  state, however, the proton occupancy indicates a sudden jump at  $N = 40$  before starting to decrease after that neutron number. Figure 7 (b) reinforces the discussion in a form of  $\Delta n(\pi p_{3/2}) = |n(\pi p_{3/2}) - n(\pi p_{3/2})_0|$ .

Thus we can explain the lowering of the excited  $0_2^+$  energy at  $N = 40$  (see Fig. 5) as a result of cooperative effects of magicity at the closed-shell configuration for proton and neutron. The magicity of the  $N = 40$  subshell gives rise to the lowering of the excited  $0_2^+$  state of the Ge isotopes at this neutron number. When protons occupy the  $p_{3/2}$  orbit at  $N = 40$ , the neutron  $p_{1/2}$  orbit is lowered due to the  $T = 0$  attractive monopole force  $V_m^{\text{PMU}}(p_{3/2}, p_{1/2}, T = 0)$  between the proton  $p_{3/2}$  and the neutron  $p_{1/2}$  orbits. This results in both increases of the neutron shell gap between the  $p_{1/2}$  and  $g_{9/2}$  orbits and the proton shell gap between the  $f_{5/2}$  and  $p_{3/2}$  orbits, which lowers the excitation energy of the first excited  $0_2^+$  state. For the Se isotopes, the calculated  $0_2^+$  energy increases at  $N = 40$ , in contrast to the experimental data. In this isotopic chain, the monopole interaction between the proton  $f_{5/2}$  orbit and neutron  $g_{9/2}$  orbit results in a decrease of the proton shell-gap at  $N = 40$  because the proton  $f_{5/2}$  and neutron  $g_{9/2}$  orbits are lowered due to this monopole force. In fact, for  $^{74}\text{Se}$  the proton  $p_{3/2}$  occupation numbers are 3.4 and 2.8 for the  $0_2^+$  and other states, respectively. The difference is not large and is about half of that for  $^{72}\text{Ge}$  (see Fig. 7 (a)). This

monopole component may be too strong for the lowering of the  $0_2^+$  state at  $N = 40$  in the Se isotopes. For the ground-state band, the neutron occupation number  $n(vg_{9/2})$  increases smoothly in Fig. 6 (a) due to the drastic increase of  $\Delta n(vg_{9/2})$ . This means that the neutron shell-gap at  $N = 40$  is washed out due to the strong pairing and quadrupole-quadrupole force. The ground-state band thus varies smoothly without showing any shell changes.

Finally, we discuss  $E2$  transition probabilities within the low-lying yrast states. Figure 8 compares the calculated  $B(E2, 2_1^+ \rightarrow 0_1^+)$  and  $B(E2, 4_1^+ \rightarrow 2_1^+)$  with available experimental data for Ni, Zn, Ge, and Se isotopes. The effective charges in the  $E2$  calculation are taken as  $e_p = 1.5$  and  $e_n = 1.1$  for protons and neutrons, respectively. The choice of a larger neutron effective charge than the standard one ( $e_n = 0.5$ ) gives a better agreement for most of the data points. There are however discrepancies. For the Ni isotopes, the calculated  $B(E2)$  values are smaller than the experimental ones except for  $N = 40$ . This could be due to the polarization effect from the  $^{56}\text{Ni}$  core. The contributions from the  $f_{7/2}$  shell may be important for enhancement of the  $B(E2)$  values. For the Zn isotopes, most experimental data are reproduced except for those near  $N = 40$ , where the calculated  $B(E2)$  values are too small. As seen from the ESPE in Fig. 3, the proton shell

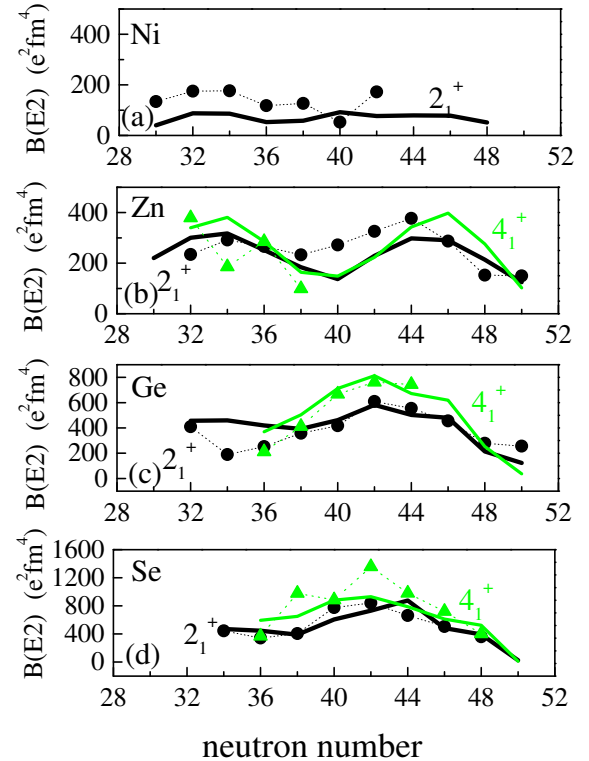


FIG. 8: (Color online) Systematics in the  $B(E2, 2_1^+ \rightarrow 0_1^+)$  and  $B(E2, 4_1^+ \rightarrow 2_1^+)$  values for Ni, Zn, Ge, and Se isotopes. The calculated results are compared with the experimental data taken from Ref. [63], where the  $2_1^+$  and  $4_1^+$  data are indicated by circles and triangles, respectively. The effective charges for proton and neutron are taken as 1.5 and 1.1, respectively.

gap between the  $p_{3/2}$  and the  $f_{5/2}$  orbits increases particularly at  $N = 40$ . The calculated small  $B(E2)$  results reflect this increase of the shell gap. The results for the Ge isotopes are overall in good agreement with the experimental data except for  $N = 34$  and  $N = 36$ , where the calculated  $B(E2)$  values are larger than the experiment. This may indicate that the shell gap between the  $p_{3/2}$  and the  $f_{5/2}$  orbits is too small in the calculation. For the Se isotopes, the calculation reproduces the experimental  $B(E2)$  values pretty well.

### B. Other low-lying states of even-even nuclei

In addition to the systematic behavior of the  $2_1^+$ ,  $4_1^+$ , and  $0_2^+$  states, other energy levels of the low-lying states in even-even nuclei are also calculated. In Fig. 9, the obtained energy levels of the low-lying negative-parity states  $3_1^-$  and  $5_1^-$  are compared with the experimental data for Ni, Zn, Ge, and Se isotopes. Although they have already been discussed in the previous subsection, the states with  $2_1^+$  and  $4_1^+$  are also given as references to show the relative energies between states with positive and negative parities. For the Ni isotopes, the calculated energy levels of the  $3_1^-$  and  $5_1^-$  states agree reasonably well with the experimental ones. Only for the light isotopes with  $N = 30$  and  $32$ , the calculated  $3_1^-$  states are slightly higher. For the Zn isotopes, the calculation reproduces the overall trend of the  $3_1^-$  and  $5_1^-$  states along the isotopic chain. Nevertheless, the calculated  $3_1^-$  levels are high for the lighter isotopes as compared to the data. Again for  $N = 30$  and  $32$  there are clear deviations of the theoretical results of  $5_1^-$  from the corresponding data. For the Ge isotopes, as already discussed, the calculation of the  $2_1^+$  and  $4_1^+$  states reproduces the known data quite well. The calculated  $3_1^-$  energies are found in good agreement with the experimental data, while the calculated  $5_1^-$  states are generally lower than the data (except for  $N = 32$ ). In Fig. 9, the calculated  $5^-$  energies generally agree with the experimental data for the Ni and Zn isotopes. An underestimation in the calculation is found only in the Ge isotopes with  $N = 34 - 38$  and the Se ones with  $N = 34, 36$ . For the Se isotopes, the systematics for the  $2_1^+$ ,  $4_1^+$ , and  $3_1^-$  states are well described by the calculation. However, the calculation seems to depart from the two data points ( $N = 34$  and  $36$ ) for the  $5_1^-$  states.

### C. Low-lying states of odd-mass nuclei

Low-lying states in odd-mass nuclei contain valuable information on the interplay between single-particle and collective motion. We now discuss energy levels of the low-lying states in odd-mass nuclei of this mass region, and try to extract information on the shell evolution along the isotopic chains. Figure 10 shows the comparison between the shell-model results and experimental data for the Ni, Zn, Ge, and Se isotopes with odd number of neutrons. The common feature for these isotopes is that the three negative-parity states,  $1/2^-$ ,  $3/2^-$ , and  $5/2^-$ , all appear near the ground state. In particular for the Ni and Zn isotopes, the experimental data indicate that these

three energy levels are nearly degenerate for  $N = 31 - 37$ . The degeneracy is lifted for heavier isotopes with  $N \geq 39$ . On the other hand, the positive-parity  $9/2^+$  state lies high in energy in the lightest isotope with  $N = 31$ , and dives down quickly as a function of neutron number. It enters into the ground-state region at  $N = 41$  (Ni and Zn) or  $39$  (Ge and Se).

As one can see in Fig. 10, our calculation reproduces the global feature correctly although for some states the agreement is only at a qualitative level. The largest deviation from the experimental data is seen for the  $1/2^-$  state in the lightest isotopes, where the calculated levels are higher than the data. The observed excitation energy for the  $5/2^-$  state increases at the neutron number  $N = 39$  and  $N = 41$ , which is well described by the calculation. The calculated  $3/2^-$  levels rise up drastically from  $N = 37$ , and lie close to the  $5/2^-$  levels for  $N \geq 41$ . For the Ge and Se isotopes, the overall variations of the low-lying states are not very drastic when neutron number increases. In all these isotopes, the calculations predict a near-degeneracy of the  $3/2^-$  and  $5/2^-$  states beyond  $N = 45$ . This degeneracy can be understood by the influence of the small difference of  $T = 1$  monopole values between  $V_m^{\text{PMMU}}(f_{5/2}, g_{9/2}, T = 1)$  and  $V_m^{\text{PMMU}}(p_{3/2}, g_{9/2}, T = 1)$ .

Another notable feature is that, as the neutron  $f_{5/2}$  orbit is occupied, the energy of the positive-parity  $9/2^+$  state goes down rapidly. This trend is correctly described by the calculation, and in particular, the  $9/2^+$  energy levels for Ge and Se isotopes are reproduced very well, as seen in Figs. 10 (c) and 10 (d). Honma *et al.* [21] has explained this trend as well from their calculations. It can be interpreted as a result of the monopole effect due to differences between  $V_m^{\text{PMMU}}(f_{5/2}, f_{5/2}, T)$  and  $V_m^{\text{PMMU}}(f_{5/2}, g_{9/2}, T)$ . For the  $9/2^+$  state, however, the agreement between our shell-model results and data becomes worse for nuclei near the closed shell. In the Ni and Zn isotopes, the calculated  $9/2^+$  states are considerably higher than the experimental ones for nuclei with  $N = 35$  and  $N = 37$ . This may be due to the large difference between  $V_m^{\text{PMMU}}(f_{5/2}, f_{5/2}, T = 0)$  and  $V_m^{\text{PMMU}}(f_{5/2}, g_{9/2}, T = 0)$ . In the Ni and Zn nuclei with  $N = 33 - 37$ , the monopole contribution disappears and the  $g_{9/2}$  ESPE goes up. This could be the reason why the calculated  $9/2^+$  states reproduce the data well for the Ge and Se nuclei, while they fail for the Ni and Zn nuclei with  $N = 35$  and  $N = 37$ .

Next, we present the results for the low-lying states of odd-mass nuclei with odd-proton and even-neutron numbers. Figure 11 shows the energy levels of odd-Z Cu, Ga, and As isotopes as functions of neutron number. As already discussed in Fig. 3, the  $5/2^-$  level comes down rapidly beyond the neutron number  $N = 40$  corresponding to the ESPE of the  $f_{5/2}$  orbit in Fig. 3 (a). The lowering of the  $5/2^-$  level can be understood as a result of the large attractive  $T = 0$  monopole term  $V_m^{\text{PMMU}}(f_{5/2}, g_{9/2}, T = 0)$  (see Fig. 2) due to the tensor force discussed in Eq. (3). In all these isotopes, the  $5/2^-$  energy levels are close to the  $1/2^-$  energy levels. This degeneracy can also be understood by the effects of the small difference of  $T = 0$  monopole values between  $V_m^{\text{PMMU}}(f_{5/2}, g_{9/2}, T = 0)$  and  $V_m^{\text{PMMU}}(p_{1/2}, g_{9/2}, T = 0)$ . The shell-model description is not successful for the  $5/2^-$  states of Cu isotopes with  $N = 30 - 40$ . This could be due to the



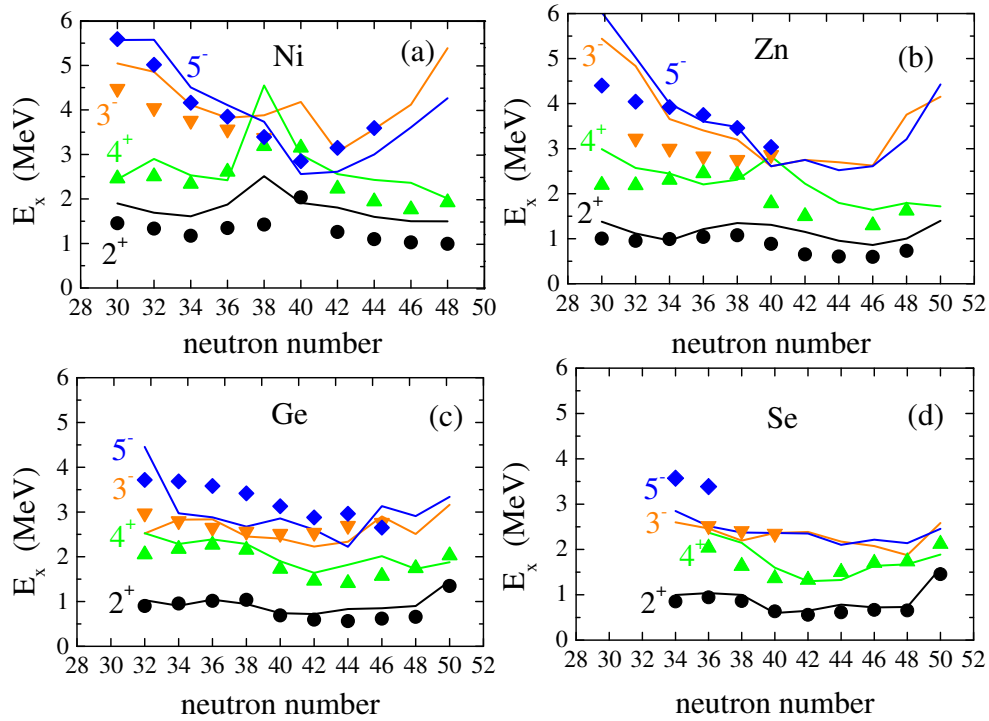


FIG. 9: (Color online) Energy levels of low-lying states for (a) Ni, (b) Zn, (c) Ge, and (d) Se isotopes with even number of neutrons. Calculated energy levels of the first  $2^+$ ,  $4^+$ ,  $3^-$ , and  $5^-$  states are shown with solid, dotted, and dot-dashed, respectively. They are compared with the experimental data denoted by circles, squares, and down-triangles. Experimental data are taken from Ref. [63].

$Z=28$  core excitations that are not included in the present calculation. We can see that the calculated results for the  $9/2^+$  states reproduce the experimental data for  $N > 40$  (with an exception for  $N = 44, 46$  Ga isotopes), while those are worse for  $N < 40$ . This may be originated from the missing effects of the  $T = 0$  monopole term between the  $f_{7/2}$  and  $g_{9/2}$  orbits. For the Ga isotopes, the calculated results for the  $1/2^-$ ,  $3/2^-$ , and  $5/2^-$  states are in good agreement with the experimental data, while for  $N = 30 - 34$  the calculated  $3/2^-$  state is higher than the experiment. The calculations for the  $9/2^+$  states reproduce well the trend of the experimental data. For the As isotopes, the energy of the  $9/2^+$  state comes down drastically and shows a minimum at  $N = 42$ . The minimum at  $N = 42$  here can be associated with the development of deformation and correlation with the  $2_1^+$  excitation energy of the doubly-even Ge and Se isotopes, as discussed in Fig. 5. The present calculations for the odd-proton As isotopes describe well such a feature.

#### D. Magnetic dipole moments and electric quadrupole moments in Cu, Ga, and Ge isotopes

In addition to energy levels, it is important to test the PMMU model further with  $E2$  transition calculations. The

magnetic moment operator is given as

$$\mu = g_s \mathbf{s} + g_l \mathbf{l}, \quad (8)$$

where  $g_s$  and  $g_l$  are the spin and the orbital  $g$ -factors, respectively. In the calculation, we employ a quenching factor 0.7 ( $g_s^{eff} = 0.7g_s^{free}$ ) for the free-nucleon spin  $g$ -factors,  $g_s^{free} = 5.586$  for protons and  $g_s^{free} = -3.826$  for neutrons. The effective charges in the electric quadrupole moment calculation are taken as  $e_p = 1.5e$  for protons and  $e_n = 1.1e$  for neutrons. Figure 12 shows the calculated results of magnetic moments and electric quadrupole moments for the Cu, Ga, and Ge isotopes. For comparison, the theoretical results for the lowest states obtained from other effective interactions, the JUN45 [21] and JJ4B interactions [21, 30], are also plotted. The calculated isotopes range from the magic number  $N = 28$  on the neutron-deficient side to  $N = 50$  on the neutron-rich side, including the semi-magic subshell closure at  $N = 40$ , where the parity change between the  $pf$  shell and the  $g_{9/2}$  orbit occurs.

In the upper graph of Fig. 12 (a), the calculated magnetic moments are shown for the Cu isotopes [66]. One can see that overall, the calculation reproduces well the experimental data. For the odd- $A$  Cu isotopes, the experimental magnetic moments of  $^{57}\text{Cu}$  and  $^{69}\text{Cu}$  are close to the effective single-particle value of the  $\pi p_{3/2}$  configuration, indicating clearly the magicity at  $N = 28$  and  $N = 40$ , respectively. The magic

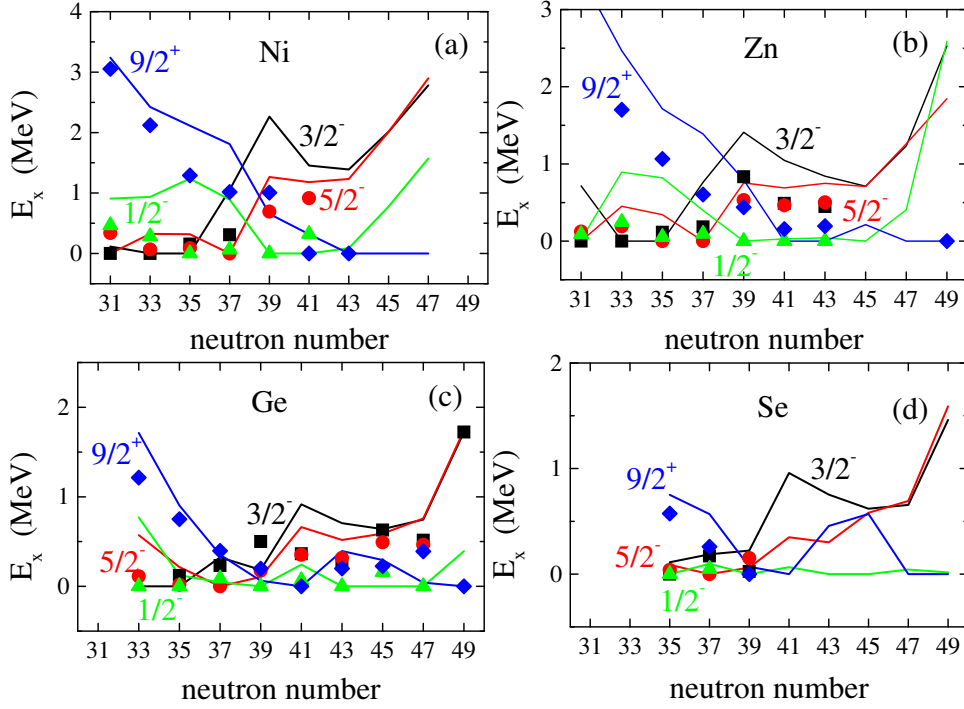


FIG. 10: (Color online) Energy levels of low-lying states for (a) Ni, (b) Zn, (c) Ge, and (d) Se isotopes with odd number of neutrons. Calculated energy levels of the first  $3/2^-$ ,  $5/2^-$ ,  $1/2^-$ , and  $9/2^+$  states are shown with solid, dotted, and dot-dashed, respectively. They are compared with the experimental data denoted by circles, squares, and down-triangles. Experimental data are taken from Ref. [63].

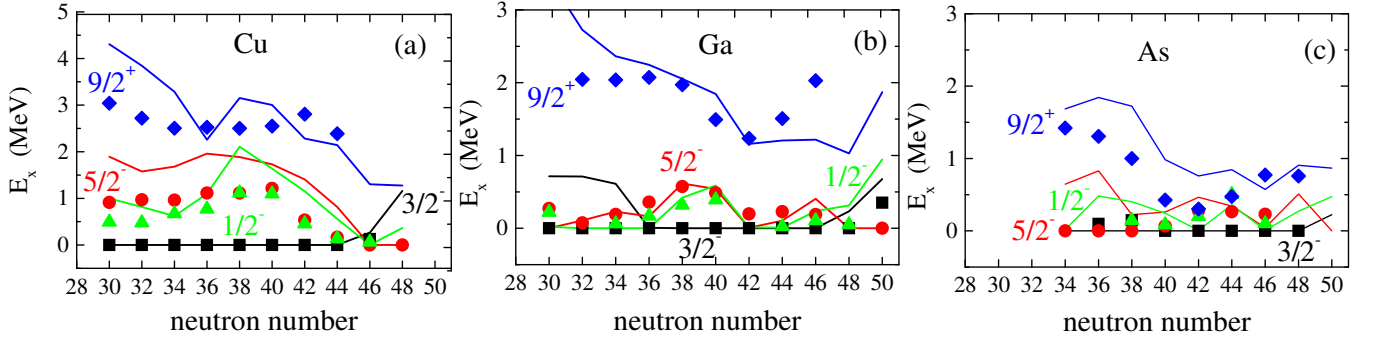


FIG. 11: (Color online) Energy levels of low-lying states for (a) Cu, (b) Ga, and (c) As isotopes with even number of neutrons. Calculated energy levels of the first  $3/2^-$ ,  $5/2^-$ ,  $1/2^-$ , and  $9/2^+$  states are shown with solid, dotted, and dot-dashed, respectively. They are compared with the experimental data denoted by circles, squares, and down-triangles. Experimental data are taken from Ref. [63].

behavior at  $N = 40$  originates from the parity exchange between the  $\nu p_{1/2}$  and  $\nu g_{9/2}$  single-particle levels, which does not allow  $M1$  excitations from the negative-parity  $pf$  shell to the positive-parity  $\nu g_{9/2}$  orbit. Some differences in magnetic moment between theory and experiment are found below  $N = 40$ , which may indicate that the  $N = 28$  shell gap is not very large, and proton excitations from the  $\pi f_{7/2}$  shell become important. Indeed, the GXPF1A calculation reproduced well the experimental magnetic moments [34]. The calculated results begin to differ largely from the experimental data for the neutron-rich side with  $N > 40$ . This could be due to the influence of the missing  $\pi f_{7/2}$  orbit. When neu-

trons begin to occupy the  $\nu g_{9/2}$  orbit, proton excitations from the  $\pi f_{7/2}$  orbit for  $N > 40$  may increase because the gap between the  $\pi f_{5/2}$  and  $\pi f_{7/2}$  orbits decreases due to the attractive  $T = 0$  monopole interaction between the  $\pi f_{7/2}$  and  $\nu g_{9/2}$  orbits. Then  $g$  factors would be better reproduced for  $N > 40$ . The calculated magnetic moments for the even- $A$  isotopes are shown in the same graph, which are found in good agreement with the data. In the lower graph of Fig. 12 (a), the calculated spectroscopic quadrupole moments are compared to the known experimental values. As one can see, a good description of the data has been achieved by the calculation for all the isotopes.

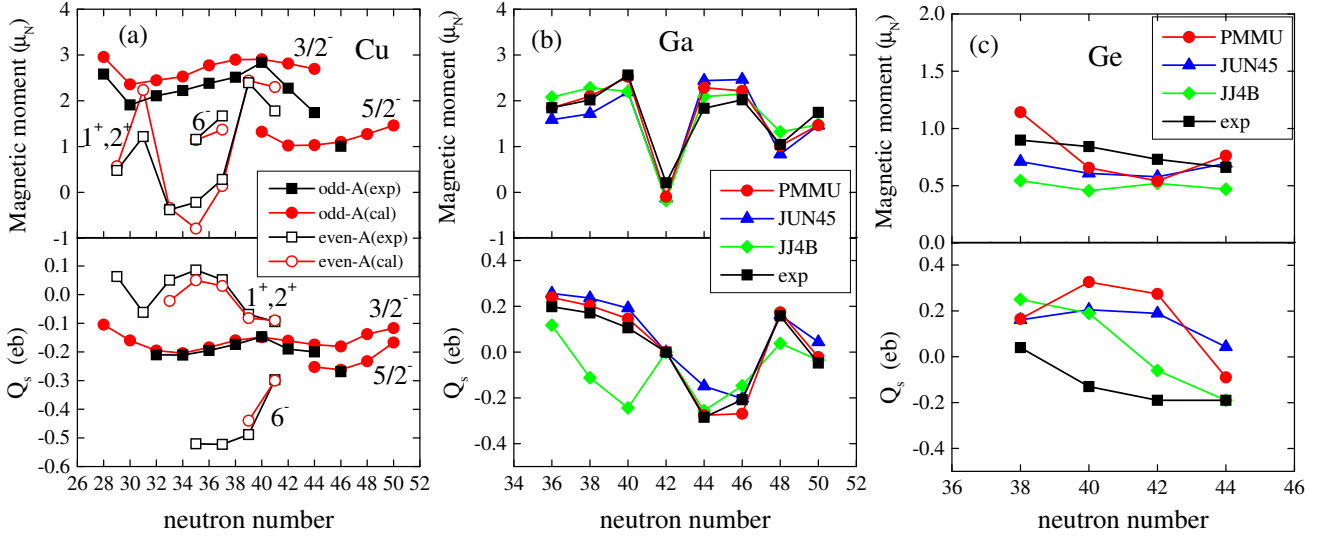


FIG. 12: (Color online) Magnetic moments and electric quadrupole moments for (a) Cu, (b) Ga, and (c) Ge isotopes. Magnetic moments with  $g_s^{eff}$ ,  $g_s^{eff} = 0.7g_s^{(free)}$ , and electric quadrupole moments with the effective charges  $e_p = 1.5e$  for proton and  $e_n = 1.1e$  for neutron. Experimental data are taken from [8, 22, 63, 66, 67].

In the upper graph of Fig. 12 (b), the calculated magnetic moments are shown for the Ga isotopes [67]. The results for  $^{67,69}\text{Ga}$  and  $^{75,77}\text{Ga}$  are smaller and larger than the effective single-particle moments  $g^{eff}(\pi p_{3/2}) = 2.96$  of the  $\pi p_{3/2}$  orbit and  $g^{eff}(\pi f_{5/2}) = 1.46$  of the  $\pi f_{5/2}$  orbit, respectively, which suggests that the ground states of these isotopes have mixed configurations. For  $^{71}\text{Ga}$  ( $N = 40$ ), the observed magnetic moment is close to the effective moment  $g^{eff}(\pi p_{3/2}) = 2.96$  of the  $\pi p_{3/2}$  orbit, thus the  $\pi p_{3/2}$  configuration with the single-proton is the leading one in the ground state. For  $^{79}\text{Ga}$ , the calculated magnetic moment of the lowest  $I = 3/2^-$  state is significantly larger than the experimental data, and the calculated quadrupole moment has opposite sign to that of the experiment. This problem can be solved if we take the calculated magnetic and quadrupole moments for the first excited  $I = 3/2^-$  state instead of the lowest one to compare with the experimental data. Then a good agreement with data for the  $I = 3/2^-$  state of  $^{79}\text{Ga}$  can be achieved, as can be seen in Fig. 12 (b). Also in the JUN45 and JJ4B calculations, the magnetic moment of the first excited state was taken to compare with experimental data. The electric quadrupole moments of the lowest excited  $3/2^-$  states are plotted in the lower graph of Fig. 12 (b). One can see that the sign inversion occurs around  $^{73}\text{Ga}$  with  $N = 42$ . The opposite sign in their quadrupole moments suggests clearly a drastically different structure. This can be understood by non-occupation of the  $\pi p_{3/2}$  orbit, because the proton  $\pi p_{3/2}$  configuration has the negative quadrupole moment. The configurations of the ground state in  $^{75,77}\text{Ga}$  have a dominant  $\pi(p_{3/2}f_{5/2}^2)$  configuration. As one can see, the JJ4B calculations for quadrupole moment fail to reproduce experimental data for  $^{69,71}\text{Ga}$ .

The calculated magnetic moments and spectroscopic quadrupole moments for the first excited  $2^+$  states of the Ge

isotopes are shown in Fig. 12 (c), and compared with experimental data [8, 22]. In the upper graph, the calculated results underestimate the measured magnetic moments, except for  $^{70}\text{Ge}$  ( $N = 38$ ). It is interesting to notice that our calculation suggests similar results as compared to the JUN45 calculations. As one shall see later, the calculated excitation spectrum is in a reasonable agreement with the experimental data. However, the quadrupole moments of the  $2_1^+$  states are not at all accounted for by all the current shell-model calculations, as seen in the lower graph of Fig. 12 (c). This remains to be a puzzle for future investigations.

## V. STRUCTURE OF EXCITED STATES IN GE AND SE ISOTOPES

In the previous section, we presented systematical results for low-lying states from the shell-model calculation. In Figs. 10 and 11, we have seen rapid changes in energy levels occurring around  $N = 40$ . In Fig. 8, the  $B(E2)$  values increase rapidly around  $N = 42$  for Ge and Se isotopes. All these can be clear signals for transitions from a near-spherical to a prolate shape. In the transitional region, a shape coexistence phenomenon would show up. The first excited  $0^+$  state,  $0_2^+$  in doubly-even nuclei, is a key measure to indicate shape coexistence, because the  $0_2^+$  state is usually the bandhead of the emerging side band. As we have already seen in Fig. 5, the energy of the  $0_2^+$  state decreases rapidly and becomes the lowest at  $N = 40$  among all isotopes. In  $^{72}\text{Ge}$ , the  $0_2^+$  state becomes notably the first excited state, lower than  $2_1^+$ . This state has been suggested to have a spherical shape from the experimental  $B(E2)$  data. As already mentioned, there have been many theoretical approaches based on the mean-field model to understand this problem [68]. The shell-model approach de-

TABLE I:  $B(E2)$  values for the positive-parity yrast states and some collective states of  $^{66}\text{Ge}$  and  $^{68}\text{Ge}$ . Experimental data are taken from Ref. [7, 63].

$J_i^\pi \rightarrow J_f^\pi$	$^{66}\text{Ge}$ [W.u.]		$^{68}\text{Ge}$ [W.u.]	
	exp	cal	exp	cal
$2_1^+ \rightarrow 0_1^+$	12.0(23)	29.0	15.3(8)	25.4
$4_1^+ \rightarrow 2_1^+$	>9.6	33.2	12.8(15)	22.4
$6_1^+ \rightarrow 4_1^+$	>1.2	36.1	12(4)	1.8
$8_1^+ \rightarrow 6_1^+$		0.0	14(3)	0.1
$2_2^+ \rightarrow 2_1^+$	16(7)	14.5	1.0(5)	29.5
$2_3^+ \rightarrow 0_1^+$	0.13(5)	0.5	0.40(5)	0.1

scribed well the  $0_2^+$  state [21]. Thus we can expect that there are significant structure changes between the lighter ( $N < 40$ ) and heavier ( $N > 40$ ) isotopes. It is thus interesting to see whether our PMMU model is applicable to the description of full spectra including high excitations. In this section, we will discuss the energy levels and the  $E2$  transitions for the Ge and Se isotopes. As already shown in Figs. 9 and 10, our shell-model calculation describes fairly well the experimental energy levels for both even-even and odd-mass isotopes. In particular, the anomalous behavior of the  $0_2^+$  states around  $N = 40$  is reproduced correctly. Of course, there are too many excited states in the calculation. Hereafter, we show only the excited energy levels and bands that may have at least some experimental indications.

### A. Even-even Ge isotopes

We start with the  $N = Z = 32$  nucleus  $^{64}\text{Ge}$ . This nucleus has been known as a typical example showing the  $\gamma$ -soft structure among the  $N = Z$  nuclei [15, 69], which was supported by

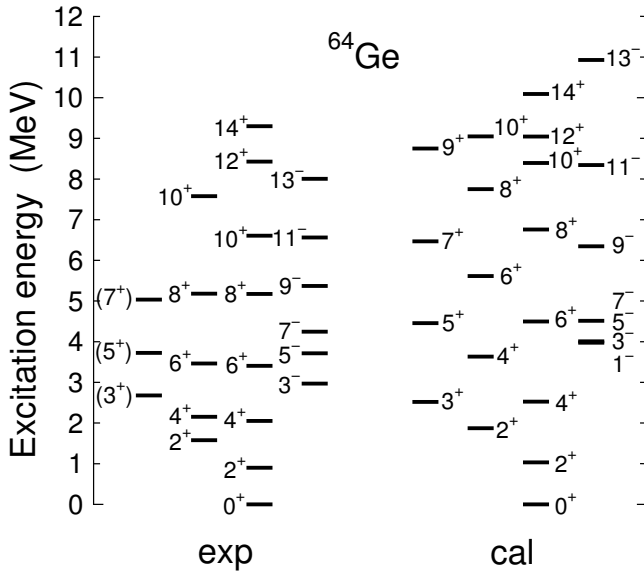


FIG. 13: Comparison of energy levels between the shell-model results and the experimental data for  $^{64}\text{Ge}$ .

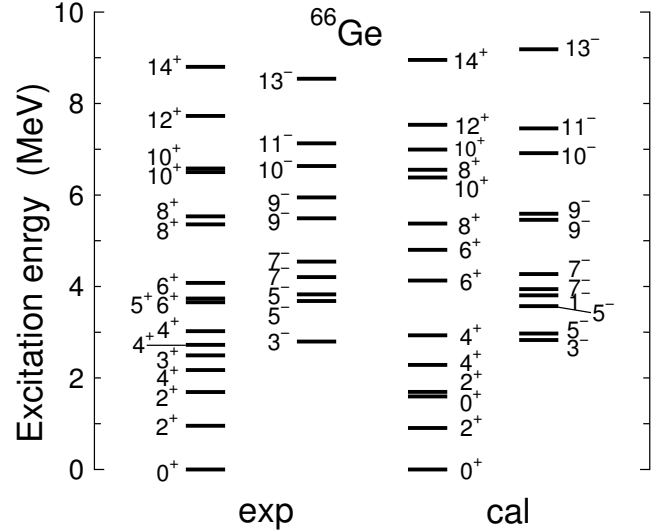


FIG. 14: Comparison of energy levels between the shell-model results and the experimental data for  $^{66}\text{Ge}$ . The experimental (calculated) energy levels are shown in the left (right) side. In each side, the first (second) line indicates the positive- (negative-) parity states. Experimental data are taken from [63].

shell-model calculations with mean-field approximation [17]. The calculation [17] predicted  $\gamma$  instability in the ground state and triaxial deformation in the excited states. Comparing our current shell-model calculations for  $^{64}\text{Ge}$  with the experimental data in Fig. 13, one can see that the low-lying states below 3 MeV are reasonably reproduced. However, the side bands for positive- and negative-parity states cannot be well described. The calculated energy levels are too high as compared to the experimental ones. This could be due to the missing  $f_{7/2}$  orbit, which is not included in the present model space.

Figure 14 shows the energy levels of the next isotope  $^{66}\text{Ge}$ . Overall, the calculation describes well the level distribution for both positive- and negative-parity states. For the positive-parity states, one finds a one-to-one correspondence between the theoretical levels and experimental ones. The  $3_1^-$  excitation energy obtained in the calculation is in good agreement with data. However, the calculated  $5_1^-$  state is predicted to be too low by about 0.8 MeV, and is almost degenerate with the  $3_1^-$  state. The two closely-lying  $7^-$  and two  $9^-$  states seen in the experiment are reasonably well reproduced. As shown in Table I, the  $E2$  transition probabilities cannot be reproduced by the calculation. The calculated  $B(E2, 2_1^+ \rightarrow 0_1^+)$  value is more than twice the observed one. Nevertheless, the  $B(E2, 2_2^+ \rightarrow 2_1^+)$  value is in good agreement with the experimental data. As seen early in Fig. 8, the theoretical  $B(E2, 2_1^+ \rightarrow 0_1^+)$  for the Ge isotopes reproduce quite well the experimental data, but those for the  $^{66}\text{Ge}$  and  $^{68}\text{Ge}$  are larger than the data.

Figure 15 shows the comparison of the  $^{68}\text{Ge}$  energy levels between our calculation and the experiment. The calculated results are overall satisfactory. We note that many experimentally-observed states for the energy range of 3 – 4

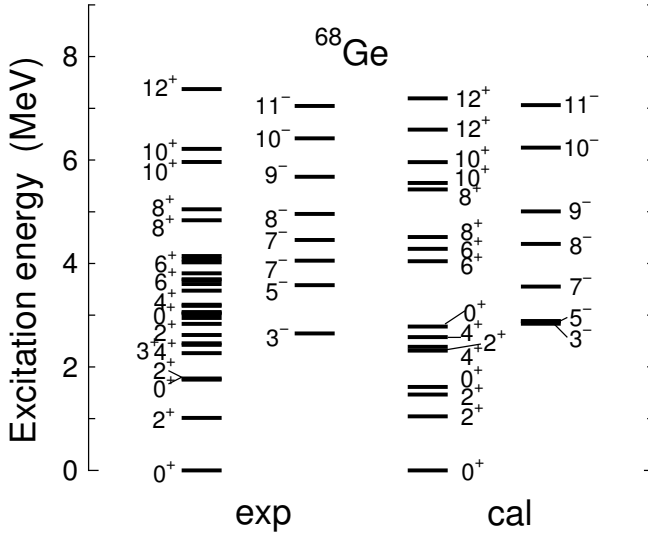


FIG. 15: Comparison of energy levels between the shell-model results and the experimental data for  $^{68}\text{Ge}$ . Experimental data are taken from [63]. Conventions are the same as those in Fig. 14.

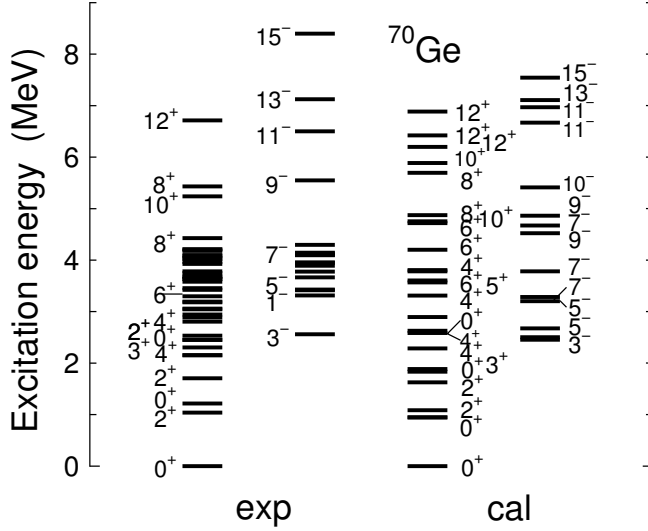


FIG. 16: Comparison of energy levels between the shell-model results and the experimental data for  $^{70}\text{Ge}$ . Experimental data are taken from [63]. Conventions are the same as those in Fig. 14.

MeV have no spin assignment. The calculation predicts the second excited  $2_2^+$  state above the known  $2_1^+$  state and the second excited  $6_2^+$  state above the known  $6_1^+$  state. On the other hand, the calculated negative-parity energy levels correspond better to the experimental ones. For electric quadrupole transitions in the positive-parity states, one sees from Table I that similar to  $^{66}\text{Ge}$ , the calculated  $B(E2, 2_1^+ \rightarrow 0_1^+)$  value is quite large as compared to the corresponding data. The calculated  $B(E2, 2_2^+ \rightarrow 2_1^+)$  is also much larger than the data. However, the calculated  $B(E2, 6_1^+ \rightarrow 4_1^+)$  and  $B(E2, 8_1^+ \rightarrow 6_1^+)$  are too small as compared to the measurement.

Calculated energy levels of  $^{70}\text{Ge}$  are presented in Fig. 16 and compared with experimental data. The known experi-

mental levels for both positive- and negative-parities below 7 MeV are taken for comparison. The calculation reproduces correctly the first excited  $0_2^+$  state as well as the  $2^+$  and  $4^+$  states. Nevertheless, different from the experiment, the calculated  $0_2^+$  state is lower than the  $2_1^+$  state. Many experimental levels in the energy range of 2 to 4 MeV have no spin assignment. The calculated higher spin states above 4 MeV with  $8^+$ ,  $10^+$ , and  $12^+$  correspond well to the observed ones. For the negative-parity states, the first excited  $3_1^-$  state is in very good agreement with the experimental data at  $\sim 2.5$  MeV, while the higher spin states  $5_1^-$ ,  $7_1^-$ , and  $10_1^-$  can find correspondence with the observed levels. The calculated  $B(E2)$  values for the positive-parity states are compared with experimental data in Table II. The agreement with data is satisfactory, however, with one exception of  $B(E2, 2_2^+ \rightarrow 2_1^+)$ , for which the measurement has large uncertainties.

Figure 17 shows energy levels of  $^{72}\text{Ge}$ . For this isotope, it is expected that the levels reflect the  $N = 40$  subshell structure. However, both the observed  $2_1^+$  and  $0_2^+$  states are lower than corresponding ones in  $^{70}\text{Ge}$ . As already seen in the systematics of Fig. 2 and discussed previously, the  $0_2^+$  state becomes lowest at  $N = 40$ . This feature is correctly described by the calculation. The calculated second excited  $0_3^+$  state at about 2 MeV is also in good agreement with the experimental data. For the positive-parity states, there is basically a one-to-one correspondence between theory and experiment up to 4 MeV, although the observed level ordering is not always reproduced. The predicted  $6^+$  and  $8^+$  states are lower than the experimental data. For the negative-parity states, the  $3_1^-$  state from the calculation is slightly lower than the data, and the  $1_1^-$  state is quite low as compared to the data. The  $E2$  transitions of the positive-parity states are shown in Table II. It is found that the calculated  $B(E2)$  values reproduce the experimental data for  $B(E2, 2_1^+ \rightarrow 0_1^+)$ ,  $B(E2, 4_1^+ \rightarrow 2_1^+)$ , and  $B(E2, 6_1^+ \rightarrow 4_1^+)$ , but not for  $B(E2, 8_1^+ \rightarrow 6_1^+)$  and  $B(E2, 2_2^+ \rightarrow 2_1^+)$ .

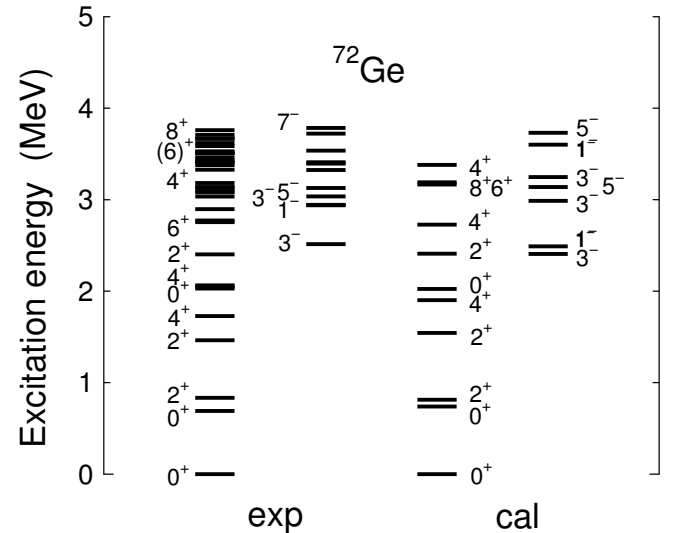


FIG. 17: Comparison of energy levels between the shell-model results and the experimental data for  $^{72}\text{Ge}$ . Experimental data are taken from [63]. Conventions are the same as those in Fig. 14.

TABLE II:  $B(E2)$  values for the positive-parity yrast states and some collective states of  $^{70}\text{Ge}$  and  $^{72}\text{Ge}$ . The experimental data are taken from [22].

$J_i^\pi \rightarrow J_f^\pi$	$^{70}\text{Ge}$ [W.u.]		$^{72}\text{Ge}$ [W.u.]	
	exp	cal	exp	cal
$2_1^+ \rightarrow 0_1^+$	21.0(4)	22.9	23.5(4)	26.0
$4_1^+ \rightarrow 2_1^+$	24(6)	29.4	37(5)	40.0
$6_1^+ \rightarrow 4_1^+$	34(7)	31.2	$36_{-31}^{+49}$	41.0
$8_1^+ \rightarrow 6_1^+$	6.5(17)	7.8	$4(3) \times 10^1$	1.7
$2_2^+ \rightarrow 2_1^+$	$1.11(60) \times 10^2$	8.0	62(11)	19.9
$2_2^+ \rightarrow 0_1^+$	25(14)	0.2	0.130(24)	1.3

TABLE III:  $B(E2)$  values for the positive-parity yrast states and some collective states of  $^{74}\text{Ge}$  and  $^{76}\text{Ge}$ . The experimental data are taken from [22].

$J_i^\pi \rightarrow J_f^\pi$	$^{74}\text{Ge}$ [W.u.]		$^{76}\text{Ge}$ [W.u.]	
	exp	cal	exp	cal
$2_1^+ \rightarrow 0_1^+$	33.0(4)	36.7	29(1)	31.7
$4_1^+ \rightarrow 2_1^+$	41(3)	51.3	38(9)	42.4
$6_1^+ \rightarrow 4_1^+$		50.7		0.7
$8_1^+ \rightarrow 6_1^+$		44.3		27.6
$2_2^+ \rightarrow 2_1^+$	43(6)	39.6	42(9)	33.7
$2_2^+ \rightarrow 0_1^+$	0.71(11)	1.7	0.90(22)	0.0

Energy levels of  $^{74}\text{Ge}$  are shown in Fig. 18. The shell-model description for this isotope is found to be reasonable. Comparing the energy levels between  $^{74}\text{Ge}$  and  $^{72}\text{Ge}$ , the  $0_2^+$  state in  $^{74}\text{Ge}$  is considerably higher than that in  $^{72}\text{Ge}$ . This feature is successfully reproduced by the calculation. For the negative-parity levels, the  $1_1^-$  state is the lowest in experiment while the theory gives  $3_1^-$ . Comparing the  $E2$  transitions between the calculation and experiment in Table III, one can

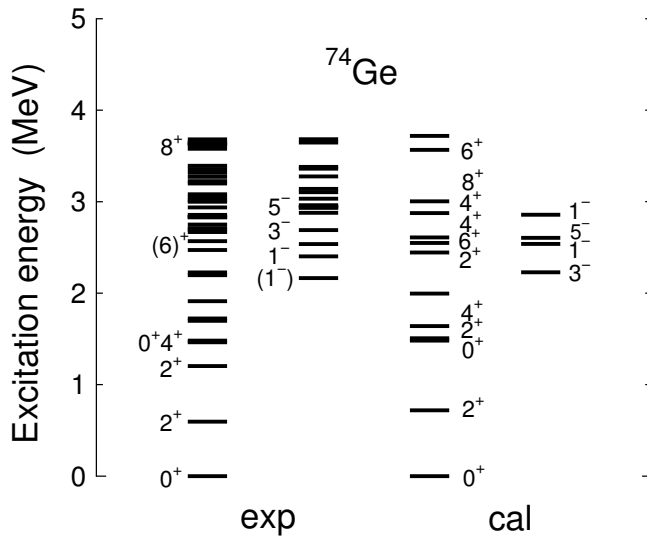


FIG. 18: Comparison of energy levels between the shell-model results and the experimental data for  $^{74}\text{Ge}$ . Experimental data are taken from [63]. Conventions are the same as those in Fig. 14.

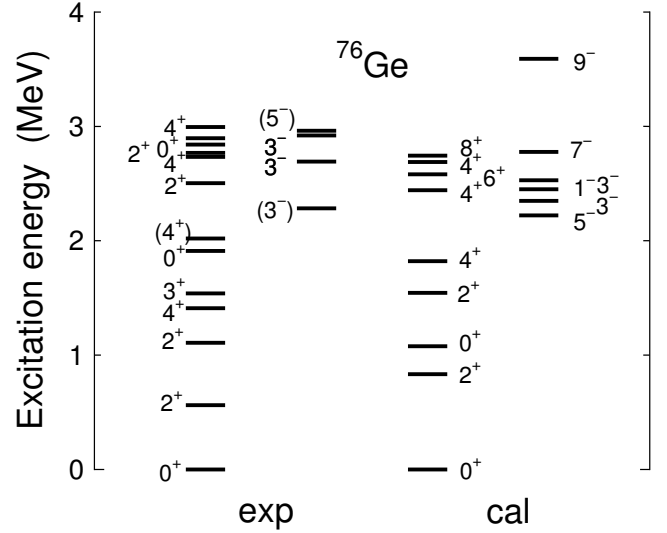


FIG. 19: Comparison of energy levels between the shell-model results and the experimental data for  $^{76}\text{Ge}$ . Experimental data are taken from [63]. Conventions are the same as those in Fig. 14.

TABLE IV:  $B(E2)$  values for the positive-parity yrast states and some collective states of  $^{69}\text{Ge}$  and  $^{71}\text{Ge}$ . The experimental data are taken from [63].

$J_i^\pi \rightarrow J_f^\pi$	$^{69}\text{Ge}$ [W.u.]		$^{71}\text{Ge}$ [W.u.]	
	exp	cal	exp	cal
$1/2_1^- \rightarrow 5/2_1^-$	0.583(25)	5.7	6.87(18)	2.1
$3/2_1^- \rightarrow 1/2_1^-$	32(23)	7.4		4.3
$3/2_1^- \rightarrow 5/2_1^-$	65(19)	21.4		15.5
$7/2_1^- \rightarrow 3/2_1^-$	12(5)	6.8		21.2
$11/2_1^+ \rightarrow 9/2_1^+$	27(4)	30.2	23(6)	29.4
$13/2_1^+ \rightarrow 9/2_1^+$	23(4)	19.1	42(9)	10.4
$9/2_1^- \rightarrow 5/2_1^-$	9.0(17)	8.0	8.7(18)	21.8
$3/2_1^+ \rightarrow 5/2_1^+$	$5_{-5}^{+7} \times 10^1$	1.3		0.1
$15/2_1^+ \rightarrow 13/2_1^+$	2.4(11)	18.0		3.7
$17/2_1^+ \rightarrow 13/2_1^+$	12.4(21)	18.3		1.8
$15/2_1^- \rightarrow 13/2_1^-$	$3_{-3}^{+4} \times 10^1$	0.0		0.2
$17/2_1^+ \rightarrow 15/2_1^+$	10(6)	0.2		12.1
$19/2_1^- \rightarrow 15/2_1^-$	8.5(10)	5.2		8.2
$21/2_1^- \rightarrow 19/2_1^-$	1.2(4)	1.1		20.4
$23/2_1^- \rightarrow 19/2_1^-$	1.86(15)	11.7		0.9

see that a reasonable agreement is obtained, although there is again a problem for  $B(E2, 2_2^+ \rightarrow 2_1^+)$ . The large  $B(E2)$  values in this isotope suggest an increasing collectivity beyond  $N = 40$ .

Energy levels of  $^{76}\text{Ge}$  are shown in Fig. 19. The observed  $0_2^+$  state lies at about 1.9 MeV, but the calculated one is found much lower than that. The first two  $2^+$  states are calculated too high as compared to the data. Nevertheless, the  $B(E2)$  values for this isotope are successfully reproduced by the calculation, as can be seen in Table III.

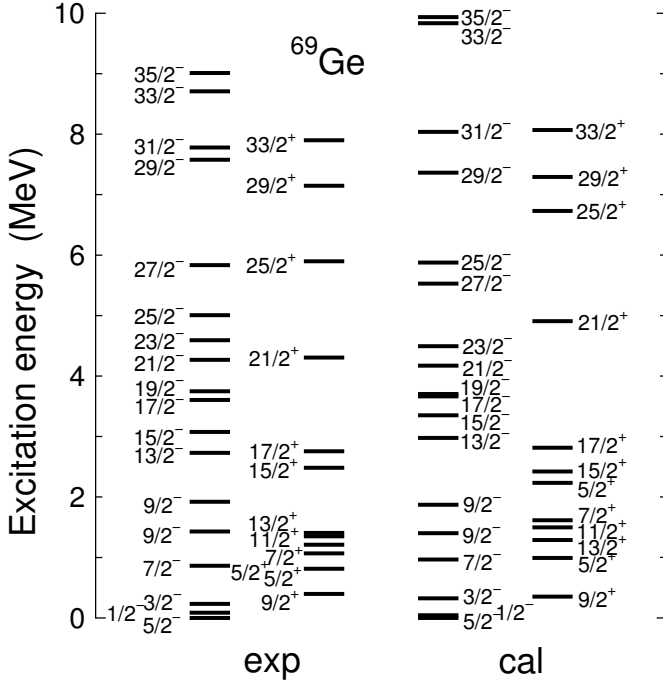


FIG. 20: Comparison of energy levels between the shell-model results and the experimental data for  $^{69}\text{Ge}$ . The experimental (calculated) energy levels are shown in the left (right) side. In each side, the first (second) line indicates the negative- (positive-) parity states. Experimental data are taken from [63].

**B. Odd-mass Ge isotopes**

We now turn our discussion on the odd-mass Ge isotopes. Figure 20 shows the energy levels of  $^{69}\text{Ge}$ . A reasonable correspondence between theory and experiment can be seen for both the negative- and positive-parity states, and up to about 8 MeV. The calculation reproduces correctly the ground state  $5/2^-$  and other nearby states. The positive-parity states are also in good agreement with data, while the second excited  $5/2^+$  state is calculated higher than the observed one. This may suggest that this state has contributions from the  $d_{5/2}$  orbit, which is not included in the present model space. The calculated highest spin states in Fig. 20, the states with  $25/2^-$ ,  $33/2^-$ , and  $35/2^-$ , are by about 1 MeV higher than the experimental data. Moreover, we find in Table IV that the most known  $E2$  transitions can be reasonably described by the current theoretical results.

For  $^{71}\text{Ge}$ , energy levels between theory and experiment are compared in Fig. 21. The calculation describes correctly the change of the ground state from the  $5/2^-$  state in  $^{69}\text{Ge}$  to the  $1/2^-$  state in  $^{71}\text{Ge}$ . The calculated level sequences are essentially similar to those of  $^{69}\text{Ge}$ , although there is no spin-parity assigned levels above 3 MeV in the experimental data. While the yrast states with negative-parity are predicted at reasonable excitation energies, the positive-parity states are not reproduced well. For example, the excited states above the lowest  $9/2^+$  state are predicted too high by the calculation. However, the behavior of the  $1/2^+$  and  $17/2^+$  doublet states

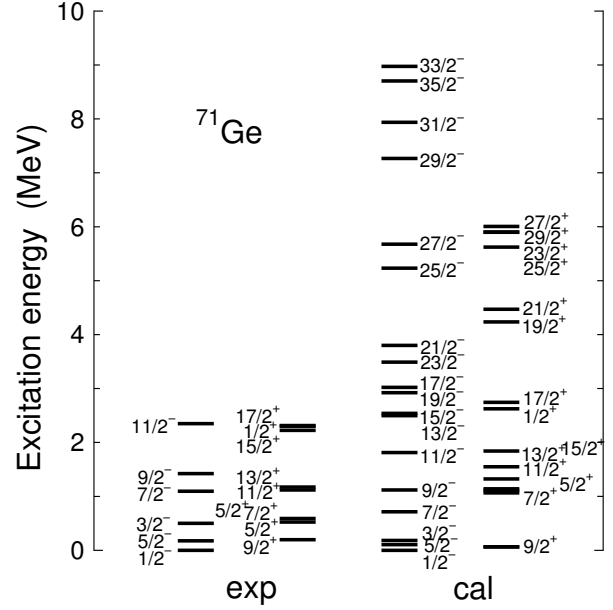


FIG. 21: Comparison of energy levels between the shell-model results and the experimental data for  $^{71}\text{Ge}$ . Experimental data are taken from [63]. Conventions are the same as those in Fig. 20.

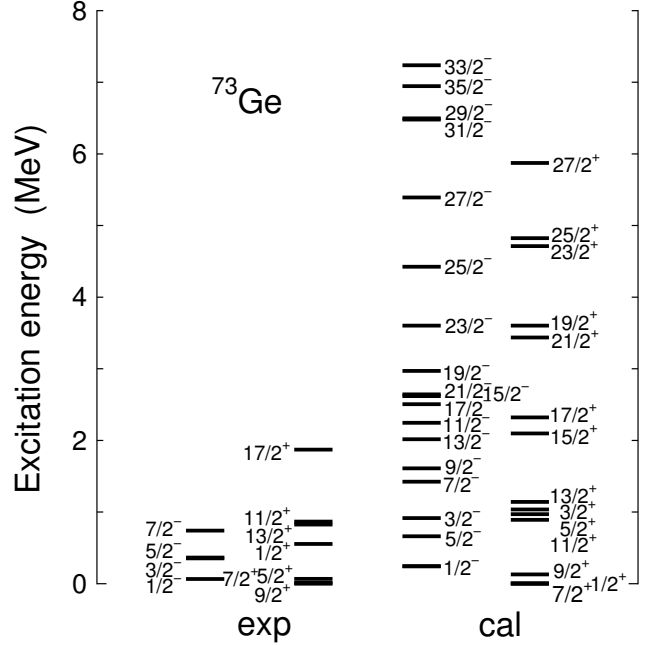


FIG. 22: Comparison of energy levels between the shell-model results and the experimental data for  $^{73}\text{Ge}$ . Experimental data are taken from [63]. Conventions are the same as those in Fig. 20.

are nicely described. In Table IV, the calculated  $B(E2)$  values are compared with the known experimental data.

As seen in Fig. 22, the shell-model results for  $^{73}\text{Ge}$  suggest the lowest-lying  $7/2^+$ ,  $1/2^+$  and  $9/2^+$  states, however, fail to reproduce the experimental ground-state spin  $9/2^+$ . The calculated  $5/2^+$  ( $1/2^+$ ) state is higher (lower) than the experimental one. The failure to describe the  $5/2^+$  state can be

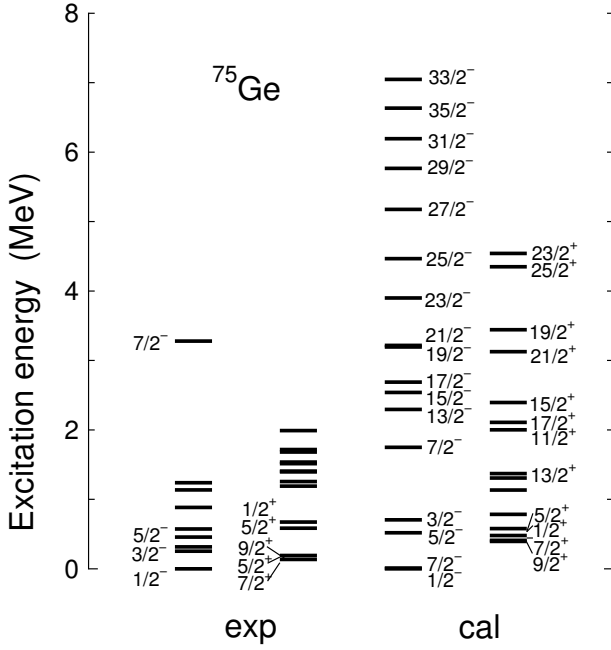


FIG. 23: Comparison of energy levels between the shell-model results and the experimental data for  $^{75}\text{Ge}$ . Experimental data are taken from [63]. Conventions are the same as those in Fig. 20.

TABLE V:  $B(E2)$  values for the positive-parity yrast states and some collective states of  $^{73}\text{Ge}$  and  $^{75}\text{Ge}$ . Non-yrast states are distinguished with their subscripts from the yrast states with no subscript. The subscript denotes a serial number for each spin  $J$ .

$J_i^\pi \rightarrow J_f^\pi$	$^{73}\text{Ge}$ [W.u.]		$^{75}\text{Ge}$ [W.u.]	
	exp	cal	exp	cal
$5/2_1^+ \rightarrow 9/2_1^+$	23.1(8)	20.5		28.4
$7/2_1^+ \rightarrow 9/2_1^+$	41(8)	48.4		44.0
$13/2_1^+ \rightarrow 9/2_1^+$	30(2)	29.5		37.8
$5/2_1^+ \rightarrow 7/2_1^+$		4.8	30(24)	18.4

systematically seen in  $^{69}\text{Ge}$  and  $^{71}\text{Ge}$ , which could be due to the missing  $d_{5/2}$  orbit in the present model space. The higher-lying yrast states  $11/2^+$ ,  $13/2^+$ , and  $17/2^+$  are reasonably reproduced, while there is no observed spectrum above 2 MeV for this isotope. For the negative-parity states, the calculated  $7/2^-$  is higher than the experimental one. The calculated  $B(E2)$  values are shown in Table V.

In Fig. 23, energy levels of the heaviest odd-mass isotope studied in this paper,  $^{75}\text{Ge}$ , are shown. Energy levels for this isotope are experimentally observed below 2 MeV. The calculation reproduces correctly the spin-parity for the ground state  $1/2^-$ . The low-lying negative-parity states  $3/2^-$  and  $5/2^-$  are reproduced reasonably. For the positive-parity states, the triplet  $9/2^+$ ,  $7/2^+$  and  $5/2^+$  states are also in good agreement with the experimental data. Since a precise level ordering for states with high density can be sensitive to the interaction matrix elements, the reproduction of the data may be accidental. As for electric quadrupole transitions, only the  $B(E2)$  value between  $7/2^+$  and  $5/2^+$  has been observed, and is in good

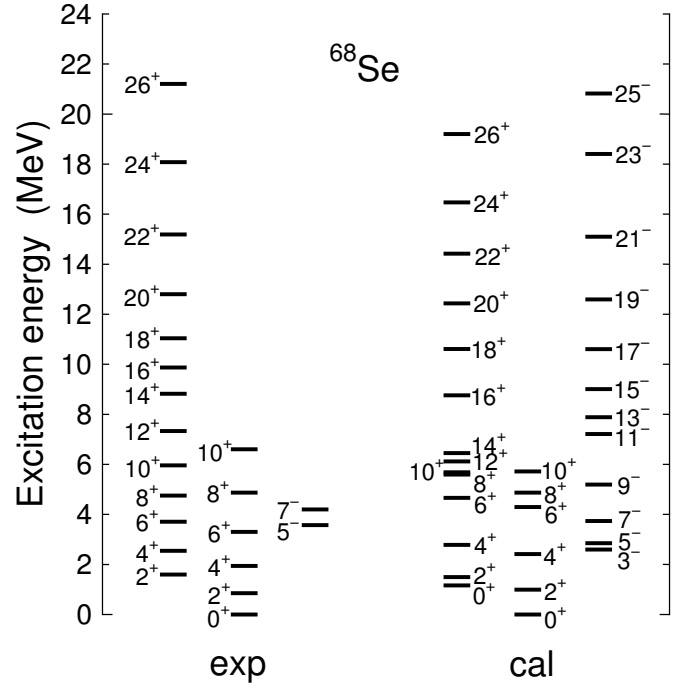


FIG. 24: Comparison of energy levels between the shell-model results and the experimental data for  $^{68}\text{Se}$ . Experimental data are taken from [63]. Conventions are the same as those in Fig. 14.

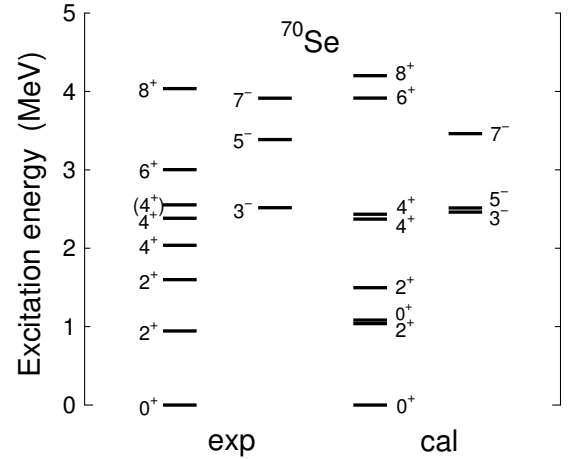


FIG. 25: Comparison of energy levels between the shell-model results and the experimental data for  $^{70}\text{Se}$ . Experimental data are taken from [63]. Conventions are the same as those in Fig. 14.

agreement with our calculation, as seen in Table V. The other  $E2$  transition probabilities are predicted.

### C. Even-even Se isotopes

The  $A \sim 70$  nuclei with  $N \sim Z$  are known to exhibit a variety of nuclear shapes. Experimental data have provided clear evidence for shape coexistence in this mass region. The ex-



TABLE VI:  $B(E2)$  values for the positive-parity yrast states and some collective states of  $^{70}\text{Se}$  and  $^{72}\text{Se}$ . The experimental data are taken from [10, 63].

$J_i^\pi \rightarrow J_f^\pi$	$^{70}\text{Se}$ [W.u.]		$^{72}\text{Se}$ [W.u.]	
	exp	cal	exp	cal
$2_1^+ \rightarrow 0_1^+$	44(9)	27.1	23.7(17)	21.9
$4_1^+ \rightarrow 2_1^+$	21(5)	34.7	55(5)	36.5
$6_1^+ \rightarrow 4_1^+$	15(4)	42.9	65(5)	48.5

perimental signature of shape coexistence is the presence of a low-lying  $0_2^+$  state. Determination of shapes was inferred indirectly from the study of rotational bands, while direct quadrupole measurements are difficult for short-lived states. The expectation of oblate deformation in this mass region was confirmed by the observation of an oblately-deformed ground-state band in  $^{68}\text{Se}$  [16]. Figure 24 shows the calculated energy levels up to high-spin states, which are compared with the known experimental data. The yrast states are fairly well described up to spin 10. The calculation predicts the first excited  $0_2^+$  state just above the second excited  $2^+$  state, while the  $0_2^+$  state is not yet observed in experiment. Our calculation supports the interpretation of an oblately-deformed rotational ground-state band in  $^{68}\text{Se}$ . The calculated  $E2$  transition strength  $B(E2; 2_1^+ \rightarrow 0_1^+) = 27.5$  W.u. is in good agreement with the experimental value 27(4) W.u.. The negative-parity  $5^-$  and  $7^-$  levels are well described.

There have been experiments that propose an oblate shape for the ground state in  $^{70}\text{Se}$  [10], while the others have reported a prolate shape [9]. There have been a number of microscopic calculations [10, 23, 26], among which the Hartree-Fock-Bogoliubov (HFB) calculation [10] predicted an oblate shape for the  $2^+$  and  $4^+$  states in the yrast band that changes to a prolate shape for the  $6^+$  state. The self-consistent collective coordinate method [26] provided a similar picture. These calculations show that the ground  $0_1^+$  state has oblate shape, the first excited  $2_1^+$  and  $4_1^+$  states have mixed the oblate-prolate configurations, and the  $6_1^+$  state has a prolate shape. Indeed, the spectroscopic quadrupole moments in the HFB calculations suggest positive values for the  $2_1^+$  and  $4_1^+$  states but a negative value for  $6_1^+$  in  $^{70}\text{Se}$  [10]. Figure 25 compares the energy levels between experiment and calculation. The calculated yrast states are in good agreement with the experimental ones, except for the  $6^+$  and  $5^-$  states. The calculation predicts the low-lying  $0_2^+$  state above the first excited  $2_1^+$  state, while the experimental one is not yet observed. In Table VI, the  $E2$  transition strengths for the  $2_1^+$ ,  $4_1^+$ , and  $6_1^+$  states are listed. The calculated  $B(E2)$  values explain fairly well the trend of variation with increasing spin  $J$ . The calculated spectroscopic quadrupole moments are 0.17, 0.49, and 0.70 eb, respectively for the  $J^\pi = 2_1^+$ ,  $4_1^+$ , and  $6_1^+$  states. Using these values and assuming an axial deformation, we can estimate the quadrupole deformation  $\beta_2$  as  $-0.10$ ,  $-0.22$ , and  $-0.28$  for the  $J^\pi = 2_1^+$ ,  $4_1^+$ , and  $6_1^+$  states, respectively, suggesting that the yrast states in  $^{70}\text{Se}$  are oblately deformed. This is consistent with the calculations in Ref. [10], except for  $J^\pi = 6_1^+$ .

$^{72}\text{Se}$  is another well-known example that exhibits an oblate-

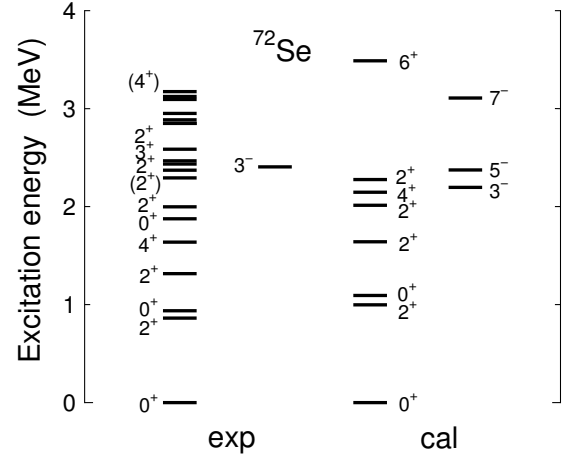


FIG. 26: Comparison of energy levels between the shell-model results and the experimental data for  $^{72}\text{Se}$ . Experimental data are taken from [63]. Conventions are the same as those in Fig. 14.

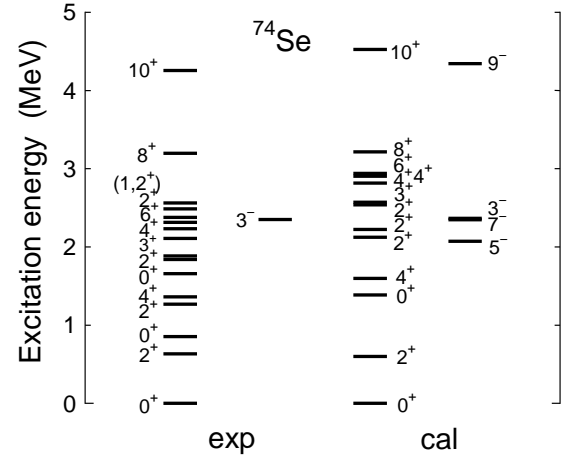


FIG. 27: Comparison of energy levels between the shell-model results and the experimental data for  $^{74}\text{Se}$ . Experimental data are taken from [63]. Conventions are the same as those in Fig. 14.

prolate shape coexistence. The ground-state band in  $^{72}\text{Se}$  in the HFB-based configuration mixing method shows a positive value of spectroscopic quadrupole moment for the  $2_1^+$  state that turns into negative for states above  $4_1^+$  [10, 11]. The present calculation suggests positive values for  $J^\pi = 2^+ - 6^+$  but a negative value for  $J^\pi = 8^+$ . The moment of inertia in the ground-state band exhibits anomalous behavior at the low-spin states of  $^{70,72}\text{Se}$ , while the high-spin states with  $J > 8$  follow a smoothly varying moment of inertia interpreted as collective rotation. Thus as  $^{70,72}\text{Se}$  rotate, their ground-state band evolves quickly into a prolate collective-rotation, while the  $2_1^+$  state can be associated with an oblate shape. The signature of shape coexistence is the presence of a low-lying first excited  $0_2^+$  state. In  $^{72}\text{Se}$ , the observed  $0_2^+$  state lies only 75 keV above the  $2_1^+$  state. As seen in Fig. 26, the calculation produces exactly the  $0_2^+$  state just above the  $2_1^+$  state. The

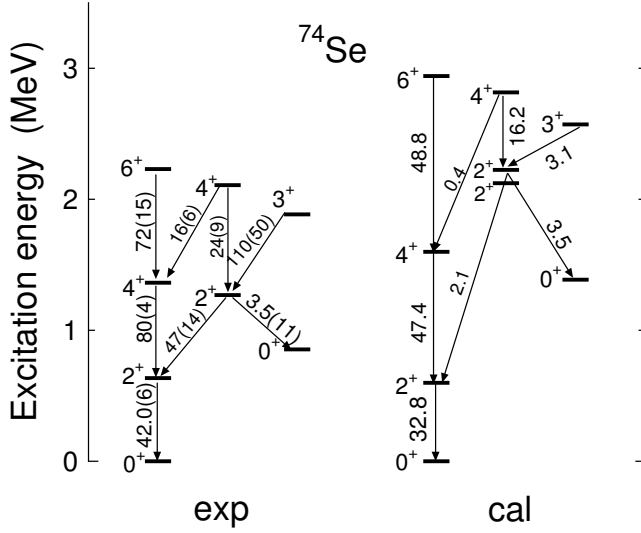


FIG. 28: Comparison of level scheme between the shell-model results and the experimental data for  $^{74}\text{Se}$ . Experimental data are taken from [63]. The numbers with the arrows represent the absolute  $B(E2)$  transition strengths (in W.u.).

calculated  $B(E2; 2_1^+ \rightarrow 0_1^+)$  is also in good agreement with the experimental data. Thus the present calculations describe well the shape coexistence in  $^{72}\text{Se}$ .

There have been many discussions on the structure of  $^{74}\text{Se}$ . Quite recently, it has been shown that the low-lying states of  $^{74}\text{Se}$  can be described as a coexistence of near-spherical and prolate shapes [12]. As seen in Figs. 27 and 28, the experimental data indicate that the  $4_1^+$ ,  $2_2^+$ , and  $0_2^+$  levels may be regarded as candidates of two-phonon states. Indeed, the  $B(E2)$  transition strengths agree well with the predictions for a spherical structure, as can be seen in Fig. 28. The small  $B(E2; 2_2^+ \rightarrow 0_2^+) = 3.5$  W.u. is consistent with the interpretation that both states are members of the two-phonon states. At high spins, the yrast states become highly deformed with a prolate shape, as the moment of inertia becomes larger. Our calculations are compared with the experimental data in Fig. 27. The results reproduce qualitatively the experimental data. Large deviations are seen for the calculated first excited  $0_2^+$  state and the first excited  $6^+$  state, which are higher in energy than the data. The  $B(E2; J \rightarrow J-2)$  values for the  $E2$  transitions de-exciting the  $J^\pi = 2_1^+$ ,  $4_1^+$ , and  $6_1^+$  states are shown in Fig. 28. These  $E2$  transitions indicate a trend of increasing magnitude with increasing spin, while the calculated magnitudes are smaller than the experimental data reported in Ref. [10, 12].

#### D. Odd-mass Se isotopes

Odd-mass Se nuclei in this mass region exhibit also rapidly-changing structures [70–72]. The study of odd-mass nuclei completes the information on the structural properties of shape-coexisting nuclei, and thus can be helpful in under-

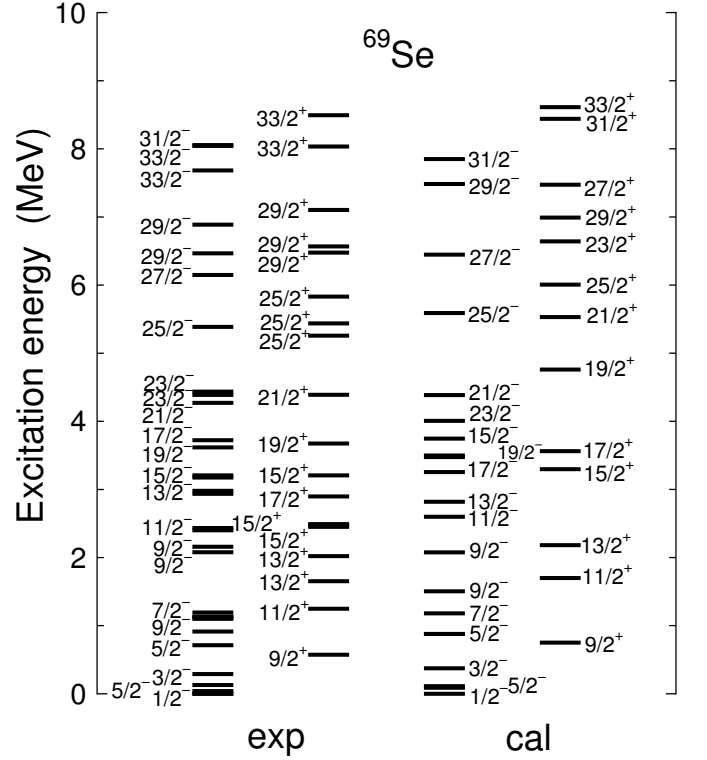


FIG. 29: Comparison of energy levels between the shell-model results and the experimental data for  $^{69}\text{Se}$ . Experimental data are taken from [63]. Conventions are the same as those in Fig. 14.

TABLE VII:  $B(E2)$  values for the positive-parity yrast states and some collective states of  $^{71}\text{Se}$  and  $^{73}\text{Se}$ . The experimental data are taken from [63, 71, 72].

$J_i^\pi \rightarrow J_f^\pi$	$^{71}\text{Se}$ [W.u.]		$^{73}\text{Se}$ [W.u.]	
	exp	cal	exp	cal
$1/2_1^- \rightarrow 5/2_1^-$	1.63(21)	1.6		6.0
$13/2_1^+ \rightarrow 9/2_1^+$	30(10)	8.7	41(4)	9.1
$17/2_1^+ \rightarrow 13/2_1^+$		8.5	140(40)	3.8
$21/2_1^+ \rightarrow 17/2_1^+$		9.4	110(30)	1.3
$5/2_1^+ \rightarrow 9/2_1^+$		10.6	22(6)	6.7

standing the effects produced by coupling of the last particle with an even-even core, which gives more insight into the interplay between oblate and prolate shapes. As one can see from the levels in Fig. 29, for  $^{69}\text{Se}$  the low-lying negative-parity states suggest a small deformation and appear to be dominated by single-particle excitations, where the  $1/2^-$  state is the ground state [70]. These states have irregular level-spacings that do not follow a rotational pattern. Our calculation reproduces nicely the ground state with correct spin and parity  $1/2^-$  and the low-lying states with  $5/2^-$  and  $3/2^-$ , as well as  $9/2^+$ . The reported experimental results [70] have confirmed that the oblate  $g_{9/2}$  band in  $^{69}\text{Se}$  is generated by coupling of the odd neutron to  $^{68}\text{Se}$ , which also has an oblate shape in the ground state. The  $9/2^+$  level is an isomeric state and the bandhead of the positive-parity band. The one-

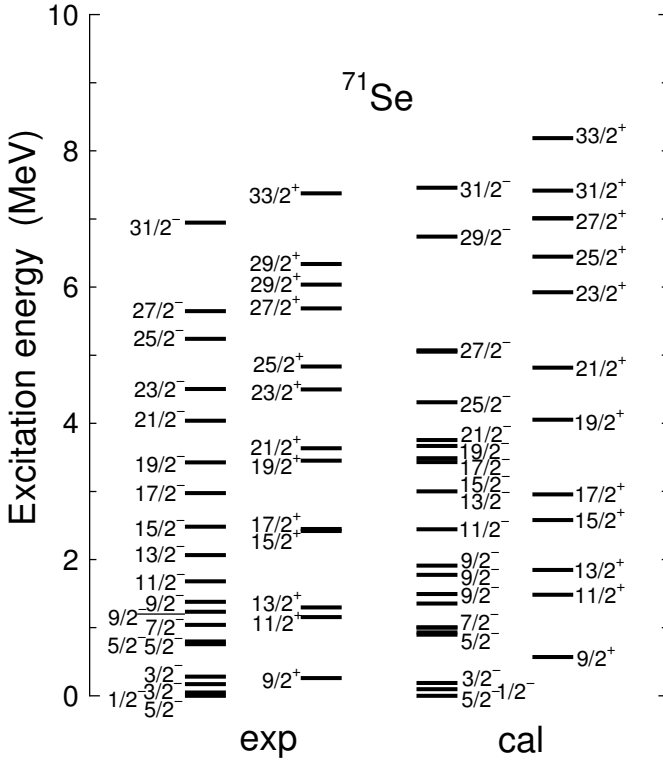


FIG. 30: Comparison of energy levels between the shell-model results and the experimental data for  $^{71}\text{Se}$ . Experimental data are taken from [63]. Conventions are the same as those in Fig. 14.

quasiparticle states of the yrast and near yrast positive-parity bands have been discussed in terms of a particle coupled to a rigid triaxial rotor model [70]. Above spin  $15/2^-$  around 3 MeV, collective excitations predominate, and can be regarded as the  $g_{9/2}$  neutron coupled to the  $3^-$ ,  $5^-$ , and  $7^-$  states of the neighboring even-even nucleus  $^{68}\text{Se}$ . The high-lying negative-parity states  $25/2^-$ ,  $27/2^-$ ,  $29/2^-$ , and  $31/2^-$  above 5 MeV can be interpreted as the  $g_{9/2}$  neutron coupled to  $8^- - 11^-$  states in  $^{68}\text{Se}$ .

The  $^{71}\text{Se}$  nucleus, lying between  $^{69}\text{Se}$  and the collective  $^{73}\text{Se}$ , represents a transitional feature in the level scheme [71]. The spin-parity assignment of  $5/2^-$  was established for the ground state, and the first excited state was observed as  $1/2^-$ . The calculations reproduce well the low-lying energy scheme. As seen in Fig. 30, the  $5/2^-$  ground state found in experiment can be reproduced by the calculation, and the  $1/2^-$  and  $3/2^-$  states are also well described. The lowest positive-parity  $9/2^+$  state is an isomer with a half-life ( $T_{1/2} = 19\mu\text{s}$ ). The high-lying states above 2 MeV are interpreted as the coupled states of a  $g_{9/2}$  neutron to the lowest  $3^-$ ,  $5^-$ , and  $7^-$  states of the  $^{70}\text{Se}$  core. Thus the  $^{71}\text{Se}$  nucleus shows transitional characters between neighboring nuclei that indicate single-particle excitations and collectivity. The  $E2$  transition probabilities between the low-lying positive-parity states are shown in Table VII. The shell-model calculation predicts smaller  $B(E2)$  values than the experimental data.

In contrast to  $^{71}\text{Se}$ ,  $^{73}\text{Se}$  has a different picture with highly

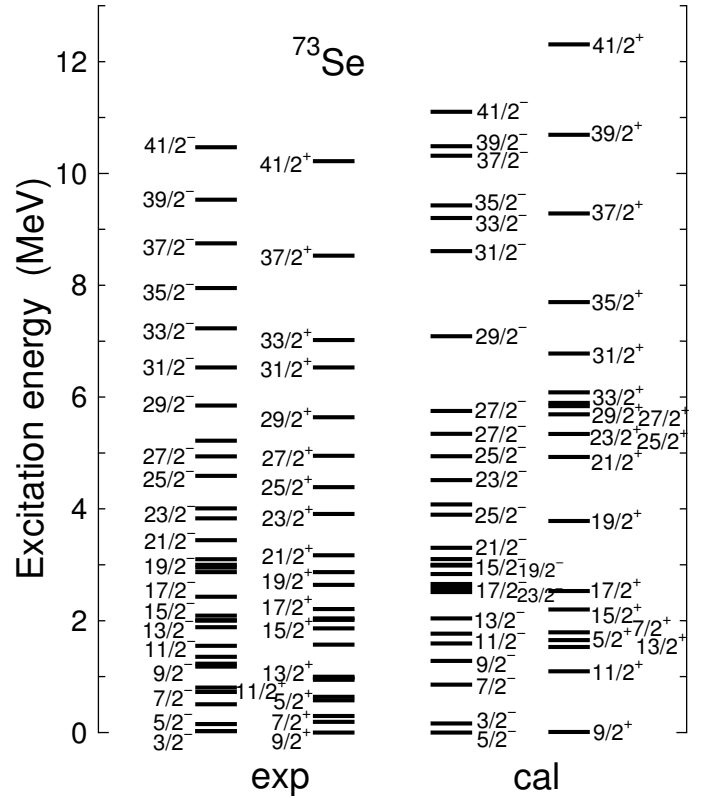


FIG. 31: Comparison of energy levels between the shell-model results and the experimental data for  $^{73}\text{Se}$ . Experimental data are taken from [63]. Conventions are the same as those in Fig. 14.

collective behavior [72]. The calculation predicts well the ground state  $9/2^+$ . The yrast positive-parity states with high spins show a collective character with large  $B(E2)$  values, as seen in Table VII. However, the calculation cannot describe these features. This may be due to the missing  $d_{5/2}$  orbit in the present model space, because the attractive  $T = 0$  monopole interaction between the  $\pi f_{5/2}$  and  $\nu d_{5/2}$  orbits would push down the  $\nu d_{5/2}$  orbit when protons occupy the  $\pi f_{5/2}$  orbit and neutrons occupy the  $\pi f_{5/2}$  orbit at high spins. The total Routhian surface (TRS) calculation for this band [73] indicated the  $\gamma$ -softness and some potential minima. Thus the shape coexistence picture found in the neighboring even-even isotopes  $^{70,72,74}\text{Se}$  persists in  $^{73}\text{Se}$ .

## VI. SUMMARY AND CONCLUSIONS

We have recently proposed a new effective interaction PMMU [53] for shell-model calculations within the  $pf_{5/2}g_{9/2}$  model space. We employ the pairing-plus-multipole Hamiltonian and adopt the monopole interaction obtained by empirical fits starting from the monopole-based universal force. For this shell model space, 14 monopole terms of  $V_m^{MU}$  are modified so as to fit energy levels,  $E2$  transitions, and binding energies for 91 nuclei in the  $pf_{5/2}g_{9/2}$  space. In the present paper, this new PMMU interaction has been examined sys-

tematically with a wide range of nuclei of the  $pf_{5/2}g_{9/2}$  mass region, from the neutron-deficient  $N = Z$  nuclei to neutron-rich ones. The calculation has been performed not only for the low-lying states, but also for high excitations for which collective rotations are dominant.

It has been demonstrated that the proposed shell model works well for most nuclei considered in the calculation, except for the Ni isotopes. Large discrepancies with the experimental data are found for the Ni isotopes. This would be due to the effects of the  $f_{7/2}$  orbit, which is not included in the present model space. The effects of the missing  $d_{5/2}$  orbit have also been discussed with the shell-model results for nuclei with neutron numbers beyond  $N = 36$ . The  $d_{5/2}$  orbit could be necessary for generating a strong collectivity in the heavier  $N = Z$  nuclei beyond the mass  $A = 72$ .

In the present paper, we have particularly studied the  $0_2^+$  state, which is the key measure of shape-coexistence. It has been found that  $0_2^+$  has an irregular behavior around the subshell at  $N = 40$ . Our shell-model calculation using the PMMU interaction has well explained the behavior of this subshell closure. We have also discussed the excited spectra of the Ge and Se isotopes in detail, and concluded that the PMMU interaction also describe the high-spin states.

As mentioned in our previous paper [53], the PMMU model could be a feasible method to unify different shell models and could extend shell-model calculations to heavier systems. In this way, one may begin to talk about universality for shell models. With the inclusion of the  $d_{5/2}$  orbit, shell-model calculations in the  $pf_{5/2}g_{9/2}d_{5/2}$  model space are in progress. We expect that the PMMU model could be applicable for the neutron-rich nuclei in the  $fp$ -shell region [44], the  $sd$ - $pf$  shell region [45], and even the heavy neutron-rich nuclei around  $^{132}\text{Sn}$  [46–48], where the pairing-plus-multipole Hamiltonian have been applied and monopole corrections have been found to be important.

### Acknowledgments

Research at SJTU was supported by the National Natural Science Foundation of China (Nos. 11135005, 11575112), by the 973 Program of China (No. 2013CB834401), and by the Open Project Program of State Key Laboratory of Theoretical Physics, Institute of Theoretical Physics, Chinese Academy of Sciences, China (No. Y5KF141CJ1).

- 
- [1] M. Bernas, Ph. Dessagne, M. Langevin, J. Payet, F. Pougheon, and P. Roussel, Phys. Lett. **113B**, 279 (1982).
- [2] R. Broda, B. Fornal, W. Królas, T. Pawlat, D. Bazzacco, S. Lunardi, C. Rossi-Alvarez, R. Menegazzo, G. de Angelis, P. Bednarczyk, J. Rico, D. De Acuña, P. J. Daly, R. H. Mayer, M. Sferrazza, H. Grawe, K. H. Maier, and R. Schubart, Phys. Rev. Lett. **74**, 868 (1995).
- [3] C. Guénaut, G. Audi, D. Beck, K. Blaum, G. Bollen, P. Delahaye, F. Herfurth, A. Kellerbauer, H.-J. Kluge, J. Libert, D. Lunney, S. Schwarz, L. Schweikhard, and C. Yazidjian, Phys. Rev. C **75**, 044303 (2007).
- [4] W. F. Mueller, B. Bruyneel, S. Franchoo, H. Grawe, M. Huyse, U. Köster, K.-L. Kratz, K. Kruglov, Y. Kudryavtsev, B. Pfeiffer, R. Raabe, I. Reusen, P. Thirolf, P. Van Duppen, J. Van Roosbroeck, L. Vermeeren, W. B. Walters, and L. Weissman, Phys. Rev. Lett. **83**, 3613 (1999).
- [5] O. Sorlin, S. Leenhardt, C. Donzaud, J. Duprat, F. Azaiez, F. Nowacki, H. Grawe, Zs. Dombrádi, F. Amorini, A. Astier, D. Baiborodin, M. Bellegruic, C. Borcea, C. Bourgeois, D. M. Cullen, Z. Dlouhy, E. Dragulescu, M. Górska, S. Grévy, D. Guillemaud-Mueller, G. Hagemann, B. Herskind, J. Kiener, R. Lemmon, M. Lewitowicz, S. M. Lukyanov, P. Mayet, F. de Oliveira Santos, D. Pantalica, Yu.-E. Penionzhkevich, F. Pougheon, A. Poves, N. Redon, M. G. Saint-Laurent, J. A. Scarpaci, G. Sletten, M. Stanoiu, O. Tarasov, and Ch. Theisen, Phys. Rev. Lett. **88**, 092501 (2002).
- [6] K. Langanke, J. Terasaki, F. Nowaki, D. J. Dean, and W. Nazarewicz, Phys. Rev. C **67**, 044314 (2003).
- [7] R. Lüttke, E. A. McCutchan, V. Werner, K. Aleksandrova, S. Atwater, H. Ai, R. J. Casperson, R. F. Casten, A. Heinz, A. F. Mertz, J. Qian, B. Shoraka, J. R. Terry, E. Williams, and R. Winkler, Phys. Rev. C **85**, 017301 (2012).
- [8] G. Gürdal, E. A. Stefanova, P. Boutachkov, D. A. Torres, G. J. Kumbartzki, N. Benczer-Koller, Y. Y. Sharon, L. Zamick, S. J. Q. Robinson, T. Ahn, V. Anagnostatou, C. Bernards, M. Elvers, A. Heinz, G. Ilie, D. Radeck, D. Savran, V. Werner, and E. Williams, Phys. Rev. C **88**, 014301 (2013).
- [9] A. M. Hurst, P. A. Butler, D. G. Jenkins, P. Delahaye, F. Wenander, F. Ames, C. J. Barton, T. Behrens, A. Bürger, J. Cederkäll, E. Clément, T. Czosnyka, T. Davinson, G. de Angelis, J. Eberth, A. Ekström, S. Franchoo, G. Georgiev, A. Gørgen, R.-D. Herzberg, M. Huyse, O. Ivanov, J. Iwanicki, G. D. Jones, P. Kent, U. Köster, T. Kröll, R. Krücken, A. C. Larsen, M. Nespolo, M. Pantea, E. S. Paul, M. Petri, H. Scheit, T. Sieber, S. Siem, J. F. Smith, A. Steer, I. Stefanescu, N. U. H. Syed, J. Van de Walle, P. Van Duppen, R. Wadsworth, N. Warr, D. Weishaar, and M. Zielińska, Phys. Rev. Lett. **98**, 072501 (2007).
- [10] J. Ljungvall, A. Gørgen, M. Girod, J.-P. Delaroche, A. Dewald, C. Dossat, E. Farnea, W. Korten, B. Melon, R. Menegazzo, A. Obertelli, R. Orlandi, P. Petkov, T. Pissulla, S. Siem, R. P. Singh, J. Srebrny, Ch. Theisen, C. A. Ur, J. J. Valiente-Dobón, K. O. Zell, and M. Zielińska, Phys. Rev. Lett. **100**, 102502 (2008).
- [11] E. A. McCutchan, C. J. Lister, T. Ahn, R. J. Casperson, A. Heinz, G. Ilie, J. Qian, E. Williams, R. Winkler, and V. Werner, Phys. Rev. C **83**, 024310 (2011).
- [12] E. A. McCutchan, C. J. Lister, T. Ahn, V. Anagnostatou, N. Cooper, M. Elvers, P. Goddard, A. Heinz, G. Ilie, D. Radeck, D. Savran, and V. Werner, Phys. Rev. C **87**, 014307 (2013).
- [13] C. J. Lister, M. Campbell, A. A. Chishti, W. Gelletly, L. Goettig, R. Moscrop, B. J. Varley, A. N. James, T. Morrison, H. G. Price, J. Simpson, K. Connel, and O. Skeppstedt, Phys. Rev. Lett. **59**, 1270 (1987).
- [14] J. Doring, G. D. Johns, M. A. Riley, S. L. Tabor, Y. Sun, and J. A. Sheikh, Phys. Rev. C **57**, 2912 (1998).
- [15] P. J. Ennis, C. J. Lister, W. Gelletly, H. G. Price, B. J. Varley, P. A. Butler, T. Hoare, S. Cwoik, and W. Nazarewicz, Nucl. Phys. **A535**, 392 (1991).

- [16] S. M. Fischer, D. P. Balamuth, P. A. Hausladen, C. J. Lister, M. P. Carpenter, D. Seweryniak, and J. Schwartz, *Phys. Rev. Lett.* **84**, 4064 (2000).
- [17] K. Kaneko, M. Hasegawa, and T. Mizusaki, *Phys. Rev. C* **70**, 051301 (2004).
- [18] A. Obertelli, T. Baugher, D. Bazin, J. -P. Delaroche, F. Flavigny, A. Gade, M. Girod, T. Glasmacher, A. Goergen, G. F. Grinyer, W. Korten, J. Ljungvall, S. McDaniel, A. Ratkiewicz, B. Sulignano, and D. Weisshaar, *Phys. Rev. C* **80**, 031304(R) (2009).
- [19] K. Kaneko, M. Hasegawa, and T. Mizusaki, *Phys. Rev. C* **66**, 051306(R) (2002).
- [20] M. Hasegawa, T. Mizusaki, K. Kaneko, and Y. Sun, *Nucl. Phys. A* **789**, 46 (2007).
- [21] M. Honma, T. Otsuka, T. Mizusaki, and M. Hjorth-Jensen, *Phys. Rev. C* **80**, 064323 (2009).
- [22] S. J. Q. Robinson, L. Zamick, and Y. Y. Sharon, *Phys. Rev. C* **83**, 027302 (2011).
- [23] A. Petrovici, K. W. Schmid, and A. Faessler, *Nucl. Phys. A* **710** 246 (2002); **728** 396 (2003).
- [24] Y. Sun, *Eur. Phys. J. A* **20**, 133 (2004).
- [25] Y. Sun, M. Wiescher, A. Aprahamian, and J. Fisker, *Nucl. Phys. A* **758**, 765 (2005).
- [26] N. Hinohara, T. Natatsukasa, M. Matsuo, and K. Matsuyanagi, *Phys. Rev. C* **80**, 041305 (2009).
- [27] Y.-C. Yang, Y. Sun, K. Kaneko, and M. Hasegawa, *Phys. Rev. C* **82**, 031304(R) (2010).
- [28] E. Padilla-Rodal, A. Galindo-Uribarri, C. Baktash, J. C. Batchelder, J. R. Beene, R. Bijker, B. A. Brown, O. Castaños, B. Fuentes, J. Gomez del Campo, P. A. Hausladen, Y. Larochelle, A. F. Lisetskiy, P. E. Mueller, D. C. Radford, D. W. Stracener, J. P. Urrego, R. L. Varner, and C.-H. Yu, *Phys. Rev. Lett.* **94**, 122501 (2005).
- [29] A. F. Lisetskiy, B. A. Brown, M. Horoi, and H. Grawe, *Phys. Rev. C* **70**, 044314 (2004).
- [30] B. A. Brown and A. F. Lisetskiy (unpublished).
- [31] T. T. S. Kuo and G. E. Brown, *Nucl. Phys. A* **114**, 241 (1968).
- [32] M. Hjorth-Jensen, T. T. S. Kuo, and E. Osnes, *Phys. Rep.* **261**, 125 (1995).
- [33] E. Epelbaum, H.-W. Hammer and U.-G. Meisner, *Rev. Mod. Phys.* **81**, 1773 (2009).
- [34] M. Honma, T. Otsuka, B. A. Brown, and T. Mizusaki, *Phys. Rev. C* **69**, 034335 (2004).
- [35] B. A. Brown and B. H. Wildenthal, *Ann. Rev. Nucl. Part. Sci.* **38**, 29 (1988).
- [36] B. A. Brown and W. A. Richter, *Phys. Rev. C* **74**, 034315 (2006).
- [37] A. Poves, J. Sanchez-Solano, E. Caurier, and F. Nowacki, *Nucl. Phys. A* **694**, 157 (2001).
- [38] S. M. Lenzi, F. Nowacki, A. Poves, and K. Sieja, *Phys. Rev. C* **82**, 054301 (2010).
- [39] S. Kahana, H. C. Lee, and C. K. Scott, *Phys. Rev.* **180**, 956 (1969).
- [40] L. S. Kisslinger and R. A. Sorensen, *Rev. Mod. Phys.* **35**, 853 (1963).
- [41] D. R. Bes and R. A. Sorensen, 'Advances in Nuclear Physics' (Plenum Press) vol. 2, 129 (1969).
- [42] M. Dufour and A. P. Zuker, *Phys. Rev. C* **54**, 1641 (1996).
- [43] M. Hasegawa, K. Kaneko, and S. Tazaki, *Nucl. Phys. A* **688**, 765 (2001).
- [44] K. Kaneko, Y. Sun, M. Hasegawa, and T. Mizusaki, *Phys. Rev. C* **78**, 064312 (2008).
- [45] K. Kaneko, Y. Sun, M. Hasegawa, and T. Mizusaki, *Phys. Rev. C* **83**, 014320 (2011).
- [46] H. Jin, M. Hasegawa, S. Tazaki, K. Kaneko, and Y. Sun, *Phys. Rev. C* **84**, 044324 (2011).
- [47] H.-K. Wang, Y. Sun, H. Jin, K. Kaneko, and S. Tazaki, *Phys. Rev. C* **88**, 054310 (2013).
- [48] H.-K. Wang, K. Kaneko, and Y. Sun, *Phys. Rev. C* **89**, 064311 (2014).
- [49] H.-K. Wang, K. Kaneko, and Y. Sun, *Phys. Rev. C* **91**, 021303(R) (2015).
- [50] T. Otsuka, R. Fujimoto, Y. Utsuno, B. A. Brown, M. Honma, and T. Mizusaki, *Phys. Rev. Lett.* **87**, 082502 (2001).
- [51] T. Otsuka, T. Suzuki, R. Fujimoto, H. Grawe, and Y. Akaishi, *Phys. Rev. Lett.* **95**, 232502 (2005).
- [52] T. Otsuka, T. Suzuki, M. Honma, Y. Utsuno, N. Tsunoda, K. Tsukiyama, and M. Hjorth-Jensen, *Phys. Rev. Lett.* **104**, 012501 (2010).
- [53] K. Kaneko, T. Mizusaki, Y. Sun, and S. Tazaki, *Phys. Rev. C* **89**, 011302(R) (2014).
- [54] A. Poves and A. Zuker, *Phys. Rep.* **70**, 235 (1981).
- [55] A. P. Zuker, *Phys. Rev. Lett.* **90**, 042502 (2003).
- [56] K. Sieja and F. Nowaki, *Phys. Rev. C* **85**, 051301(R) (2012).
- [57] T. Otsuka, T. Suzuki, J. D. Holt, A. Schwenk, and Y. Akaishi, *Phys. Rev. Lett.* **105**, 032501 (2010).
- [58] C. Yuan, T. Suzuki, T. Otsuka, F. Xu, and N. Tsunoda, *Phys. Rev. C* **85**, 064324 (2012).
- [59] Y. Utsuno, T. Otsuka, B. A. Brown, M. Honma, T. Mizusaki, and N. Shimizu, *Phys. Rev. C* **86**, 051301 (2012).
- [60] T. Togashi, N. Shimizu, Y. Utsuno, T. Otsuka, and M. Honma, *Phys. Rev. C* **89**, 024320 (2015).
- [61] R. K. Bansal and J. B. French, *Phys. Lett.* **11**, 145 (1964).
- [62] T. Mizusaki, N. Shimizu, Y. Utsuno, and M. Honma, code MSHELL64 (unpublished).
- [63] Data extracted using the NNDC World Wide Web site from the ENDSF data base.
- [64] G. Audi, A. H. Wapstra, and C. Thibault, *Nucl. Phys. A* **729**, 337 (2003).
- [65] B. J. Cole, *Phys. Rev. C* **59**, 726 (1999).
- [66] P. Vingerhoets, K. T. Flanagan, M. Avgoulea, J. Billowes, M. L. Bissell, K. Blaum, B. A. Brown, B. Cheal, M. De Rydt, D. H. Forest, Ch. Geppert, M. Honma, M. Kowalska, J. Krämer, A. Krieger, E. Mané, R. Neugart, G. Neyens, W. Nörtershäuser, T. Otsuka, M. Schug, H. H. Stroke, G. Tungate, and D. T. Yordanov, *Phys. Rev. C* **82**, 064311 (2010).
- [67] B. Cheal, E. Mané, J. Billowes, M. L. Bissell, K. Blaum, B. A. Brown, F. C. Charlwood, K. T. Flanagan, D. H. Forest, C. Geppert, M. Honma, A. Jokinen, M. Kowalska, A. Krieger, J. Krämer, I. D. Moore, R. Neugart, G. Neyens, W. Nörtershäuser, M. Schug, H. H. Stroke, P. Vingerhoets, D. T. Yordanov, and M. Záková, *Phys. Rev. Lett.* **104**, 252502 (2010).
- [68] M. Bender, P. Bonche, and P.-H. Heenen, *Phys. Rev. C* **74**, 024312 (2006).
- [69] M. Hasegawa, K. Kaneko, T. Mizusaki, and Y. Sun, *Phys. Lett. B* **656**, 51 (2007).
- [70] I. Stefanescu, J. Eberth, G. de Angelis, N. Warr, G. Gersch, T. Steinhardt, O. Thelen, D. Weisshaar, T. Martinez, A. Jungclaus, R. Schwengner, K. P. Lieb, E. A. Stefanova, D. Curien, and A. Gelberg, *Phys. Rev. C* **69**, 034333 (2004).
- [71] A. R. Howe, R. A. Haring-Kaye, J. Döring, N. R. Baker, S. J. Kuhn, S. L. Tabor, S. R. Arora, J. K. Bruckman, and C. R. Hoffman, *Phys. Rev. C* **86**, 014328 (2012).
- [72] R. Lortz, O. Iordanov, E. Galindo, A. Jungclaus, D. Kast, K. P. Lieb, C. Teich, F. Cristancho, Ch. Ender, T. Härtlein, F. Köck, D. Schwalm, *Eur. Phys. J. A.* **6**, 257 (1999).
- [73] M. S. Kaplan, J. X. Saladin, D. F. Winchell, H. Takai, and J. Dudek, *Phys. Rev. C* **44**, 668 (1991).